JGR Oceans

RESEARCH ARTICLE
10.1029/2024JC021194

Large Eddy Simulation of Cross-Shore Hydrodynamics Under Random Waves in the Inner Surf and Swash Zones

Benjamin Tsai[1], Tian-Jian Hsu[2], Seok-Bong Lee[3], Maria Pontiki[2], Jack A. Puleo[2], and Meagan E. Wengrove[4]

[1]U.S. Geological Survey, St. Petersburg Coastal and Marine Science Center, St. Petersburg, FL, USA, [2]Center for Applied Coastal Research, Department of Civil and Environmental Engineering, University of Delaware, Newark, DE, USA, [3]School of Ocean Science and Engineering, University of Southern Mississippi, Stennis Space Center, Bay St. Louis, MS, USA, [4]Department of Civil and Construction Engineering, Oregon State University, Corvallis, OR, USA

Abstract A 3D large eddy simulation coupled with a free surface tracking scheme was used to simulate cross-shore hydrodynamics as observed in a large wave flume experiment. The primary objective was to enhance the understanding of wave-backwash interactions and the implications for observed morphodynamics. Two simulation cases were carried out to elucidate key processes of wave-backwash interactions across two distinct stages: berm erosion and sandbar formation, during the early portion of a modeled storm. The major difference between the two cases was the bathymetry: one featuring a berm without a sandbar (Case I), and the other, featuring a sandbar without a berm (Case II) at similar water depth. Good agreement (overall Willmott's index of agreement greater than 0.8) between simulations and measured data in free surface elevation, wave spectrum, and flow velocities validated the model skill. The findings indicated that the bottom shear stress, represented by the Shields parameter, was significant in both cases, potentially contributing substantial sediment transport. Notably, the occurrence of intense wave-backwash interactions were more frequent in the absence of a sandbar. These intense wave-backwash interactions resulted in a pronounced horizontal pressure gradient, quantified by high Sleath parameters, exceeding the criteria for momentary bed failure. Additionally, a more vigorous turbulence-bed interaction, characterized by near-bed turbulent kinetic energy, was observed in the case lacking a sandbar, potentially augmenting sediment suspension. These insights are pivotal in understanding the mechanisms underlying berm erosion and how sandbar formation serves to protect further beach erosion.

Plain Language Summary Computer simulations that mimic real-world nearshore waves in a large wave flume were used to understand how waves and the beach interact, especially for beach shape during storm impact. Simulations accuracy was verified by comparing output with the experiment data, including changes of the water surface, wave patterns, and the speed of flow. We studied the interactions between waves and the beach for two different beach shapes. First, we studied the beach before a storm characterized by a raised area called a berm at the shoreline. Then, we studied the beach during a storm, where the berm disappears but an underwater sandbar forms seaward from the shoreline. Comparing the two scenarios helped us understand how beaches change during different stages of a storm. We found that between the two, the way that the water moved along the bottom was different, which may cause distinct ways of sand movement. When there is no sandbar, the offshore-directed flow following after wave breaking interacts more strongly with incoming waves. This process leads to significant changes in horizontal pressure and turbulent activity, possibly causing more movement of sand. Our findings help us better understand why berms erode and how sandbars might help protect the beach from erosion.

Key Points:

- The 3D large eddy simulation is validated by near-prototype scale wave flume data for random waves
- Strong wave-backwash interaction leads to a large Sleath parameter and near-bed turbulence
- The absence of a sandbar favors the occurrence of strong wave-backwash interaction events

Correspondence to:

B. Tsai,
benjamintsai@usgs.gov

Citation:

Tsai, B., Hsu, T.-J., Lee, S.-B., Pontiki, M., Puleo, J. A., & Wengrove, M. E. (2024). Large eddy simulation of cross-shore hydrodynamics under random waves in the inner surf and swash zones. *Journal of Geophysical Research: Oceans*, *129*, e2024JC021194. https://doi.org/10.1029/2024JC021194

Received 11 APR 2024
Accepted 7 SEP 2024

Author Contributions:

Conceptualization: Tian-Jian Hsu, Jack A. Puleo
Data curation: Seok-Bong Lee, Maria Pontiki
Formal analysis: Benjamin Tsai
Funding acquisition: Tian-Jian Hsu, Jack A. Puleo, Meagan E. Wengrove
Investigation: Benjamin Tsai
Supervision: Tian-Jian Hsu
Writing – original draft: Benjamin Tsai
Writing – review & editing: Tian-Jian Hsu, Seok-Bong Lee, Maria Pontiki, Jack A. Puleo, Meagan E. Wengrove

1. Introduction

Sea level rise and extreme weather caused by climate change have become a major societal concern. It would be advantageous to incorporate their impacts into the design of coastal protection and resource management. Beaches are the first line of defense against storms. However, beach profiles are highly dynamic and they can change dramatically during storms. Coastal morphodynamics are shaped by the complex interplay among bathymetry, waves, currents, turbulence, and sediment transport. The understanding and ability to quantify interactions between hydrodynamics and bathymetry remain limited in inner surf and swash zones where intense sediment transport and rapid morphodynamics occur.

Numerical models for coastal processes are useful tools to gain understanding and insight into complex systems and serve as a complement to field and laboratory experiments. Wave modeling approaches can be classified into two major categories, wave-resolving and wave-averaged models, and some further apply depth-integration (Liu & Losada, 2002). Wave-averaged models, such as WAVEWATCH (Tolman, 1991) and SWAN (Booij et al., 1999), rely on empirical formulas to parameterize many unresolved key processes, such as wave breaking, and nonlinear wave evolution (wave skewness and asymmetry). For morphodynamic modeling, surfbeat models such as XBeach (surbeat version, Roelvink et al., 2009) and COAWST (coupled with InWave-ROMS model, Olabarrieta et al., 2023) have become popular as they are hybrid-models with the incident sea-swell waves modeled as wave-averaged formulations while resolving the low frequency (infragravity) waves. Wave-resolving models, such as Boussinesq-type depth-integrated wave models, for example, MIKE21 (Madsen & Sørensen, 1992) and FUNWAVE (G. Wei et al., 1995) and non-hydrostatic depth-resolving wave models, for example, SWASH (Zijlema et al., 2011) and NHWAVE (Ma et al., 2012) are developed to better predict nonlinear wave transformation. However, these models treat the free surface as a single value function, meaning that they can at best capture shocks, but are not able to resolve wave over-turning and subsequent wave breaking. Thus, parameterizations for the wave breaking induced turbulence are required since the vertical variation of turbulence further affects undertow profiles (Derakhti et al., 2016).

The need for parameterizing the roller dissipation and the wave breaking generated turbulence in the aforementioned models has introduced additional uncertainties into nearshore wave modeling and the related coastal processes, such as sediment transport. With growing computational resources, models with less parameterizations, computational fluid dynamics (CFD), are increasingly being used to study surf zone processes. CFD models can be classified as either mesh-based or mesh-free. Mesh-free models include the Smoothed Particle Hydrodynamics method, which has successfully been used to study nearshore waves (Altomare et al., 2023; Lowe et al., 2019; Z. Wei et al., 2017). This study focuses on mesh-based models which incorporate free surface tracking techniques (e.g., the volume of fluid (VOF) method (Hirt & Nichols, 1981) or the level set method (Sussman et al., 1994)) to reconstruct the free surface. Numerical models solving Reynolds-averaged Navier–Stokes (RANS) equations parameterize all scales of turbulent fluctuations with a turbulence closure scheme. They generally require a lower computational cost relative to turbulence-resolving models, such as the large eddy simulation (LES). A variety of turbulent closure models for RANS has been applied for nearshore processes with the k-ε (Bradford, 2000; Brown et al., 2016; Higuera et al., 2013; Lin & Liu, 1998; Xie, 2013) and k-ω (Brown et al., 2016; Higuera et al., 2013; Jacobsen et al., 2012; Mayer & Madsen, 2000) two-equation turbulence closures being most popular. Among these RANS model studies, there is a collective tendency of an over-prediction of turbulence level prior to wave breaking which limits the use of RANS for long time-scale computation or for regions that are not fully turbulent (Larsen & Fuhrman, 2018). This persistent issue can affect coastal hydrodynamics simulations (e.g., wave height, undertow profile). More recently, Larsen and Fuhrman (2018) proved that nearly all two-equation models are unconditionally unstable in the potential flow region beneath (non-breaking) surface waves which leads to the generation of unphysical turbulence. The realizable k-ε model (Shih et al., 1995) is an exception that was shown to be conditionally unstable in such regions (Fuhrman & Li, 2020). A reformulation of the eddy viscosity closure in two-equation models has been suggested and the stabilized models have shown improvement in predicting turbulence and the undertow profile (Larsen & Fuhrman, 2018; Larsen et al., 2020). However, the predicted turbulence in the inner surf zone remains less satisfactory even with the stabilized models (Li et al., 2022). In this study, the research effort was extended by utilizing a three-dimensional (3D) LES approach.

With the increasing use of LES, many studies have successfully simulated wave transformation and breaking. The turbulence structure under different breaker types in the surf zone has been investigated (Christensen, 2006; Christensen & Deigaard, 2001; Lakehal & Liovic, 2011; Watanabe et al., 2005) and some studies specifically focused on air entrainment during wave breaking (Derakhti & Kirby, 2014; Lubin et al., 2006). Zhou et al. (2014) simulated a solitary wave breaking event and carried out a detailed analysis of the wave breaking-induced turbulent coherent structures (TCS) interacting with the bed. Later, a more complex bathymetry (i.e., the presence of a sandbar) was introduced to the simulations (Zhou et al., 2017) and the effect of wave breaking induced TCS on bed shear stress and sediment suspension events were analyzed statistically. However, most of the aforementioned studies focused on individual wave breaking events or a small number of monochromatic waves and none of them extended the study to the swash zone.

The swash zone plays a crucial role in active beach accretion and erosion processes. When a wave breaks, the incoming bore swashes on the beach face, leading to intense sediment transport (Puleo et al., 2000). A swash event encompasses both onshore and offshore flows on the beach face, referred to as uprush and backwash, respectively. Swash motions strongly interact with the berm, a vital coastal feature on the foreshore. Under mild wave conditions, onshore sediment transport prevails. The onshore sediment transport ultimately achieves an equilibrium state, resulting in a berm on the foreshore. A LES study carried out by Kim et al. (2017) provides insights into swash zone hydrodynamics for a single swash event generated by a dam-break wave (O'Donoghue et al., 2010). Their results show that turbulent characteristics are different from those in the surf zone due to the limited water depth during swash, consistent with earlier laboratory studies (Sou et al., 2010).

The interaction between the backwash flow and incoming waves in the inner surf zone and swash zone has been identified as a key process driving major sediment transport events (Alsina et al., 2012; Cáceres & Alsina, 2012; Hughes & Moseley, 2007). As an incoming wave approaches the swash zone, the swash flow from the previous wave reverses and rushes offshore. This backwash flow encounters the incoming wave, broken or not, with varying relative intensities, resulting in a highly dynamic and complex swash zone (Hughes & Moseley, 2007). As this cycle constantly repeats, different beach morphodynamic responses are observed (Alsina et al., 2012). In addition, a recent field study by Florence et al. (2022) observed vertical pore pressure gradients in the inner surf zone that exceeded the liquefaction criteria. These measurements were made during the passage of a breaking wave/bore, which occurred shortly after a significant decrease in water level within a large wave trough. Laboratory experiments also showed that the backwash flow and its interaction with the incoming wave may cause the formation of a hydraulic jump, and drive flow separation near the bed (Pujara et al., 2015; Sou & Yeh, 2011; Sumer et al., 2013). Although wave-backwash interaction is important, it remains difficult to quantify such interaction and how the wave breaking-driven turbulence influences near-bed sediment transport and beach profile evolution for different stages of the beach profile evolution.

To address the research gap, this study adopts LES to simulate a near-prototype scale wave flume experiment for inner surf and swash zone processes driven by random waves over the measured high resolution bathymetry. This study aims to evaluate the capability of LES to represent more realistic cross-shore hydrodynamics by using a comprehensive model validation with measured data. Simulation data are further analyzed to provide a better understanding of wave-backwash interactions, and their implication for sediment transport and cross-shore beach profile evolution.

2. Methodology

2.1. Model Formulations

A 3D air-water interface-resolving LES approach was adopted to resolve wave shoaling and breaking in the nearshore. The governing equations comprise the filtered continuity equation and momentum equations, written as:

$$\frac{\partial u_i}{\partial x_i} = 0 \tag{1}$$

and

$$\frac{\partial \rho u_i}{\partial t} + \frac{\partial \rho u_i u_j}{\partial x_j} = -\frac{\partial p}{\partial x_i} + \frac{\partial}{\partial x_j}\left(\rho \nu \frac{\partial u_i}{\partial x_j}\right) + \frac{\partial \tau_{ij}^{sgs}}{\partial x_j} + \rho g_i + \sigma \kappa \frac{\partial \alpha}{\partial x_i} \tag{2}$$

in which u_i denotes the filtered (resolved) fluid velocity and x_i stands for the Cartesian coordinates with the subscripts $i, j = 1, 2, 3$ indicating the x, y, and z directions, respectively while p and τ_{ij}^{sgs} represent the pressure and sub-grid stress. Fluid density and viscosity are indicated by ρ and ν while g_i corresponds to gravitational acceleration. The last term in Equation 2 signifies the surface tension force. Here, σ denotes the surface tension coefficient of the air-water interface and is set to be 0.07 kg/s^2 (Jacobsen et al., 2012). The surface curvature, denoted by κ, is defined as $\kappa = -\partial n_i / \partial x_i$ (n_i signifies the normal vector of the interface). For air-water modeling, α denotes the volumetric concentration of water with $\alpha = 1$ corresponding to full occupation by water and $\alpha = 0$

corresponding to full occupation by air. Any intermediate value between 0 and 1 represents a mixture of air and water which is located around the air-water interface.

For sub-grid stress, the most commonly used Smagorinsky model (Smagorinsky, 1963) is utilized in this study to parameterize unresolved sub-grid turbulent motions. As such, τ_{ij}^{sgs} is modeled as follows:

$$\tau_{ij}^{sgs} = 2\rho\nu^{sgs}S_{ij} \tag{3}$$

where S_{ij} is the strain rate tensor of the resolved velocity field defined as $S_{ij} = \frac{1}{2}\left(\frac{\partial u_i}{\partial x_j} + \frac{\partial u_j}{\partial x_i}\right)$ and ν^{sgs} represents the subgrid-scale viscosity calculated as:

$$\nu^{sgs} = (C_s\Delta)^2\sqrt{2S_{ij}S_{ij}} \tag{4}$$

in which C_s is the Smagorinsky coefficient set to be 0.167 in this study and the filtering length $\Delta = \sqrt[3]{\Delta x\Delta y\Delta z}$ is the characteristic grid size in which Δx, Δy and Δz are the grid size in x, y and z directions, respectively.

The interface between two immiscible fluids, namely air and water, is resolved using the VOF method (Hirt & Nichols, 1981). The fluid properties in the numerical model, including velocity, density, and viscosity, are obtained by a weighted average of the air and water phases. In this study, the density of water, ρ^w is set as 1000 kg/m^3 and the density of air, ρ^a, is 1 kg/m^3. Similarly, the viscosity of water, ν^w, is set to 10^{-6} m^2/s and the viscosity of air, ν^a, is set to 1.48×10^{-5} m^2/s. The surface compression method (Berberović et al., 2009; Rusche, 2002) is applied. This enhancement contributes to preserving the interfaces during the evolution. An in-depth discussion of the surface compression method can be found in Rusche (2002) and Berberović et al. (2009). The numerical implementation employed here aligns with methodologies utilized in several preceding studies, including Jacobsen et al. (2012), Zhou et al. (2014), and Kim et al. (2017).

The aforementioned formulations are adopted using the open-source CFD toolbox, `OpenFOAM`. Among various `OpenFOAM` solvers, `waves2Foam` (Jacobsen et al., 2012), a solver based on `interFoam`, is utilized which has the capability built-in to generate water waves. The boundary conditions of the model, particularly the surface wave generation and absorption method for the numerical wave flume will be discussed in Section 2.3.

2.2. Physical Experiments

A series of wave flume experiments, referred to as DUNE3, were conducted at the Large Wave Flume in the O.H. Hinsdale Wave Research Laboratory, Oregon State University, USA. The initial beach profile for this experiment was obtained by scaling a beach profile from Mantoloking, New Jersey, USA prior to Hurricane Sandy. Beach sand from Newport, Oregon, USA was used during the experiment with a median grain diameter (d) of 0.21 mm and the specific gravity (s) of 2.67. The scaling process followed van Rijn et al. (2011) with the geometry scaling factor being approximately 2.8 and the temporal scaling factor being approximately 1.7.

Hurricane Sandy was chosen as the forcing condition to mimic beach erosion during a storm. The rising limb of the storm hydrograph (i.e., water level, wave height, and wave period) was selected and discretized into 47 individual wave trials with each containing 300 irregular waves (Figure 1). A piston-type wavemaker with a built-in active absorption system was used during the experiment. The Texel-Marsen-Arsloe (TMA) wave spectrum (Bouws et al., 1985) was used to generate random waves during each trial.

Profile surveys were taken between each trial (Figure 2a) using the combination of a multiple transducer array (MTA) for measuring underwater bathymetry and a lidar system for subaerial topography. A concrete slab was placed at the offshore end of the profile as a reference point for the MTA and for sediment containment. A large number of sensors was deployed in the wave flume. The data used in this study includes those measured by capacitance wave gauges and ultrasonic distance meters for free surface elevation, acoustic Doppler velocimeters (ADV) and acoustic Doppler profiling velocimeters for flow velocity (Figure 2b). Additional details of the physical experiment can be found in Innocenti et al. (2021), Feagin et al. (2023), Pontiki et al. (2023), and Bond et al. (2023).

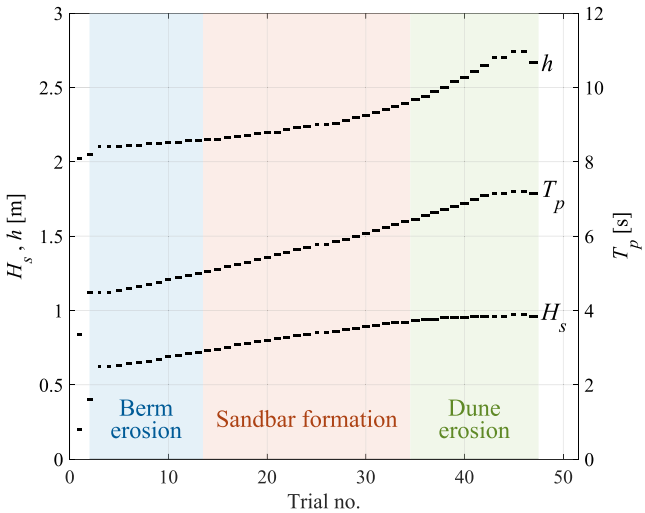

Figure 1. Hydrograph of the designed wave conditions in the DUNE3 experiment for significant wave height (H_s), peak wave period (T_p), the water level (h).

The 47 trials were categorized into three stages: berm erosion and initial sandbar formation (trial no. 1–13), sandbar growth and offshore migration (trial no. 14–35), and dune erosion (trial no. 36–47). Based on the storm impact scale (Sallenger, 2000), the berm erosion and sandbar formation stages fall into the swash regime in which the wave runup does not reach the dune foot. On the other hand, the dune erosion stage would fall into the collision regime. This study aimed to investigate the role of wave-backwash interaction and the implication to berm erosion. For this purpose, trials no. 5 and no. 20, representing the berm erosion and sandbar formation stages respectively, were selected to be simulated. Here, the two simulations are referred to as Cases I and II, respectively.

2.3. Model Setup

The numerical model domain had a length of 85 m, a width of 3.66 m, and a height of 5 m similar to the physical experiment (Figure 3). The x-direction denotes the wave propagation direction (cross-shore direction, positive landward) with $x = 0$ defined at the inlet boundary of the numerical domain. The z-direction is parallel to gravitational acceleration (positive upward) with $z = 0$ defined at the bottom of the wave flume. The y-direction denotes the alongshore direction of the flume. Using `waves2Foam` (Jacobsen et al., 2012) to set up the numerical wave flume, the first 21 m of the numerical domain is a relaxation zone that acts like a sponge layer to absorb reflected waves from the shoreline. The relaxation zone mimics the active absorption system of the wavemaker. The bed elevation in the relaxation zone was set to be the same as the height of the concrete slab in the experiment ($z = 0.17$ m). The top boundary was specified as zero-gradient for velocity and pressure.

A series of irregular waves was generated from the inlet boundary. A reflected waves filtering method similar to Zelt and Skjelbreia (1992), which uses multiple gauges and includes higher-order harmonics, was applied to

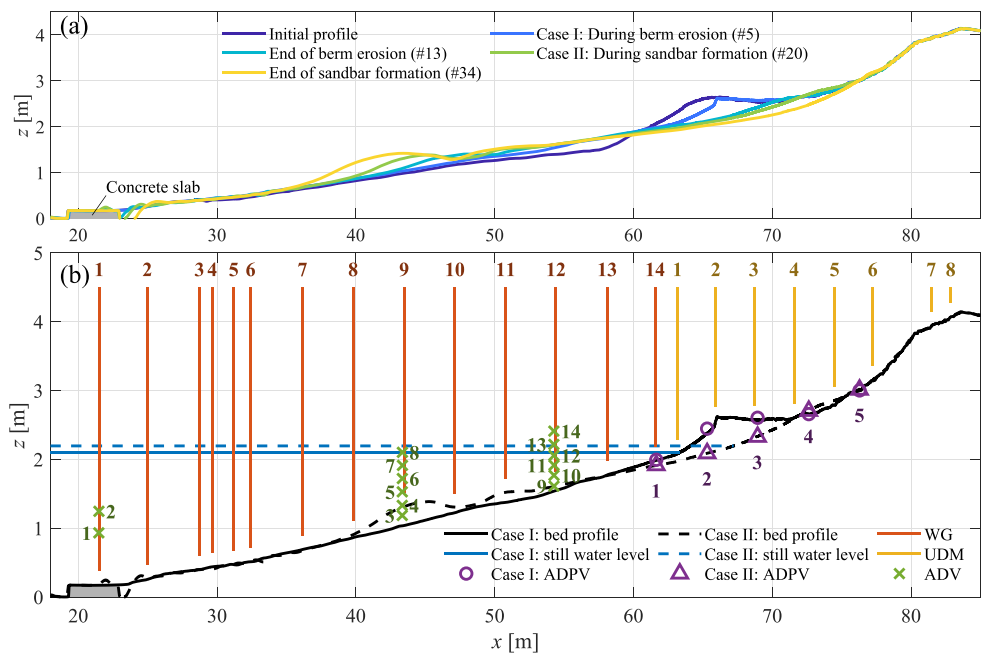

Figure 2. (a) Beach profiles from the physical experiment during the berm erosion stage (trials no. 1–13) and sandbar formation stage (trials no. 13–34). (b) Sensors locations (capacitance wave gauges, ultrasonic distance meters, acoustic Doppler velocimeters, and acoustic Doppler profiling velocimeters), beach profiles, and still water depth used in of Cases I and II.

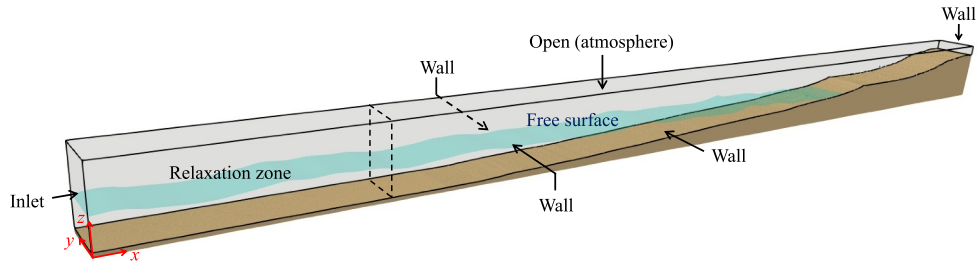

Figure 3. Schematic plot of the numerical wave flume and boundary condition applied. The computational domain includes a 21 m long relaxation zone extended from the inlet boundary. The beach profile is the bottom of the model domain and is modeled as a fixed wall.

approximate the incident waves at the inlet boundary. Details can be found in Tsai (2023). Measured data from WG1, WG2, WG5, and WG6 (x_m = 21.51, 24.98, 31.20, 32.42 m), were used to obtain the incident wave time series at the location of the wave generator ($x = 0$). The resulting incident wave time series was then specified as the inlet boundary condition to generate waves during the simulations.

Typical LES models refine the mesh near the wall boundary down to the wall unit of 1 to fully resolve the viscous sublayer (i.e., wall-resolved LES). However, wall-resolved LES requires an enormous amount of grid points in these highly turbulent and near prototype-scale simulations. Therefore, the near-wall modeling approach was applied to all wall boundaries. The near-wall model is used to obtain estimation of the wall shear stress by assuming the velocity profile follows a certain law of the wall. In this study, the sediment bed was assumed to be fixed and followed a logarithmic law for rough walls (Cebeci & Bradshaw, 1977), and so did the rough concrete side walls. The formulations are written as:

$$u^+ = \frac{1}{\kappa}\ln\frac{Ez^+}{f_n} \tag{5}$$

$$f_n = \begin{cases} 1 & , \text{if } K_s^+ \le 2.25 \\ \left(\dfrac{K_s^+ - 2.25}{87.75} + c_s K_s^+\right)^{\sin\left(0.4258\,\ln K_s^+ - 0.3453\right)} & , \text{if } 2.25 < K_s^+ < 90 \\ 1 + c_s K_s^+ & , \text{if } K_s^+ \ge 90 \end{cases} \tag{6}$$

where f_n is the roughness function that depends on the nondimensional parameter K_s^+, $c_s = 0.5$ is the roughness constant, κ is the von Kármán constant being 0.41, and E is an empirical coefficient specified to be 9.8. The nondimensional parameters expressed in terms of wall unit are defined as $z^+ = z_p u_\tau/\nu$, $u^+ = u_p/u_\tau$, and $K_s^+ = K_s u_\tau/\nu$. The friction velocity u_τ was estimated using wall-normal height from the wall (z_p), near wall velocity perpendicular to the wall (u_p), and sand-grain roughness height (K_s). K_s was specified to be $2.5d$ in this study.

A 3D unstructured mesh is adopted to develop a boundary-fit mesh for the beach profile (Figure 4). The unstructured mesh allows local refinements to cover regions requiring higher resolution (i.e., free surface and near-bed region). Background mesh size is specified as $12 \times 12 \times 4$ cm^3. A local refinement with a grid size of $6 \times 6 \times 2$ cm^3 around the free surface is specified to better capture the geometry of wave evolution. Finally, a bottom-fitted local refinement along the bed with a three-layer $3 \times 3 \times 0.333$ cm^3 mesh is adopted. The total numbers of grid points for Cases I and II are 8.19 and 8.74 million, respectively.

3. Model Validations

Cases I (trial no. 5, h = 2.10 m, H_s = 0.58 m, T_p = 4.54 s) and II (trial no. 20, h = 2.20 m, H_s = 0.72 m, T_p = 5.43 s) were chosen for a comprehensive model validation in this section. In the physical experiment, time series of free surface elevations were recorded at 22 locations along the wave flume (Figure 2b). Flow velocity was measured at eight different cross-shore locations including five ADPVs deployed close to the bed in the inner

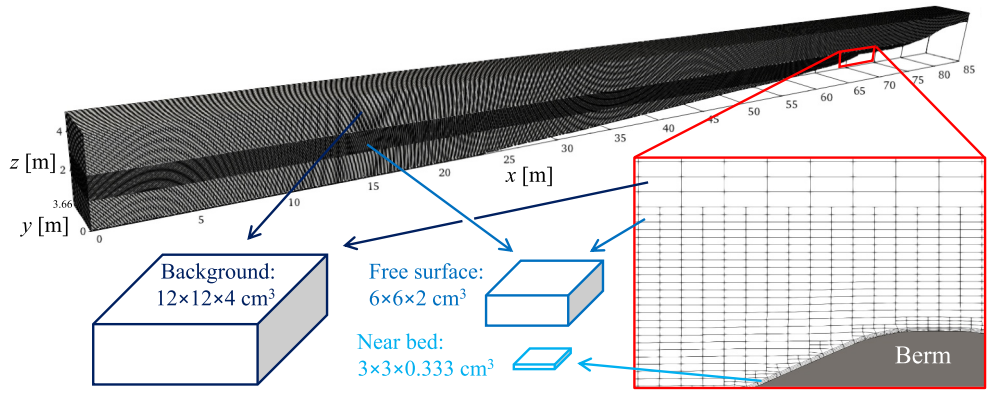

Figure 4. The mesh of the numerical domain for Case I. A similar mesh is used for Case II.

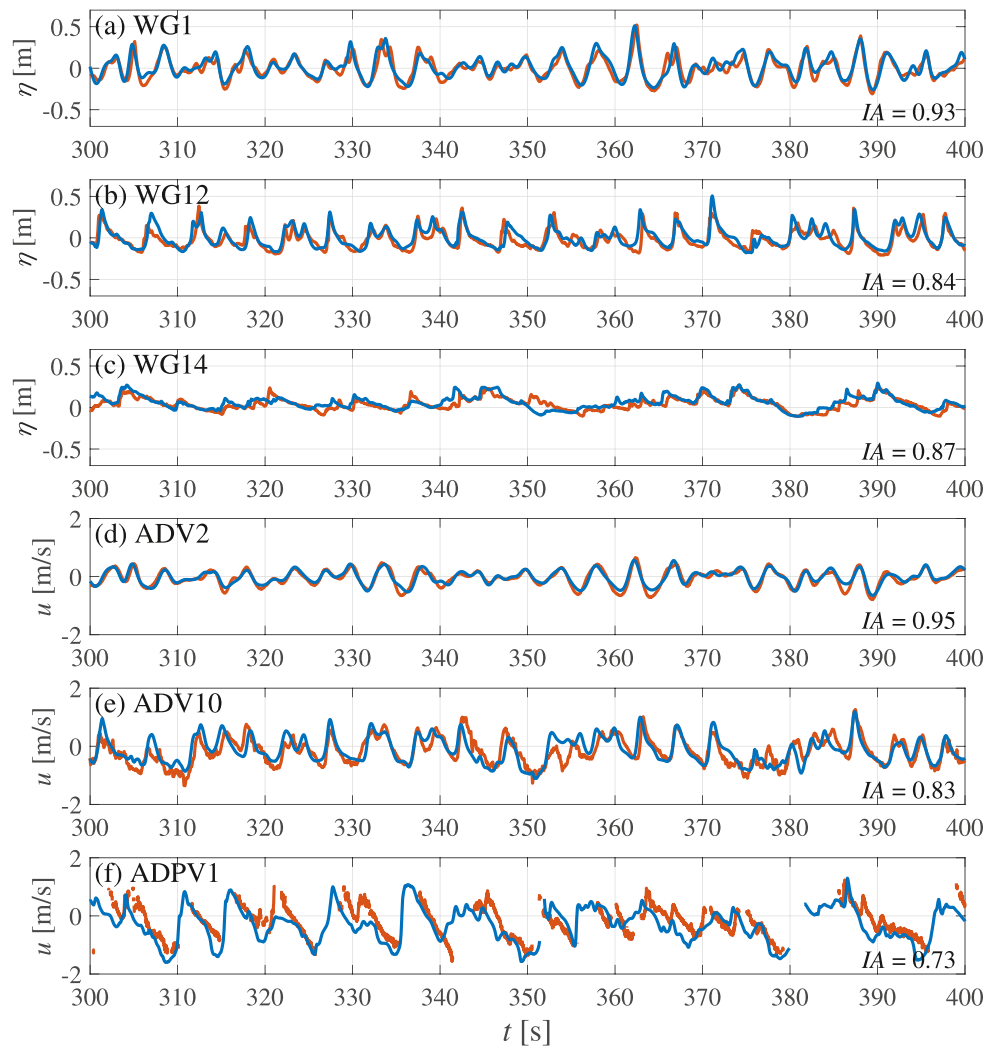

Figure 5. Comparison of time series data between model results (blue lines) and observations (orange lines) for Case I. Panels from the top (a) to bottom (f) denote WG1 (x = 21.512 m), WG12 (x = 54.416 m), WG14 (x = 61.561 m), ADV2 (x = 21.478 m), ADV10 (x = 54.271 m), and ADPV1 (x = 61.641 m).

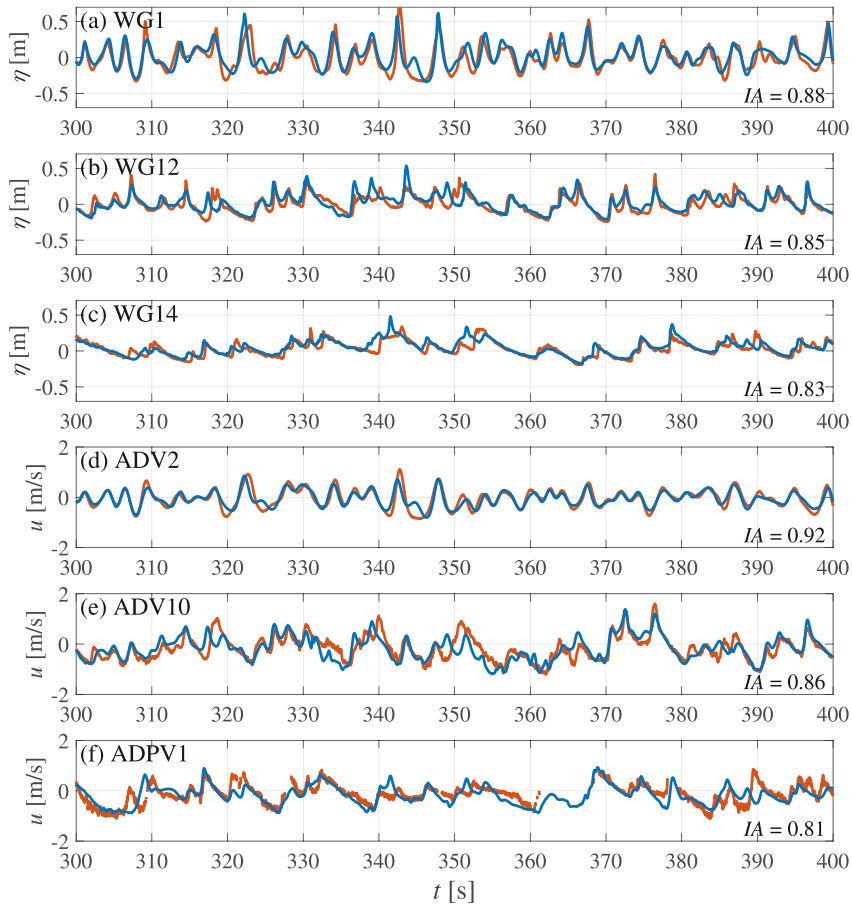

Figure 6. Comparison of time series data between model results (blue lines) and observations (orange lines) for Case II. Panels from the top (a) to bottom (f) panel denote WG1 (x = 21.512 m), WG12 (x = 54.416 m), WG14 (x = 61.561 m), ADV2 (x = 21.478 m), ADV10 (x = 54.271 m), and ADPV1 (x = 61.641 m).

surf and swash zones and three ADV arrays at offshore locations. Comparison of the selected time series of free surface elevations and flow velocities are shown in Figures 5 and 6. A standardized measure, the index of agreement (*IA*) (Willmott, 1981), is used to quantify the model performance as:

$$IA = 1 - \frac{\sum_{i=1}^{n} (P_i - O_i)^2}{\sum_{i=1}^{n} \left(|P_i - \bar{O}| + |O_i - \bar{O}|\right)^2} \tag{7}$$

in which P_i is the model prediction and O_i is the observations from $i = 1$ to n data points. The advantage of *IA* is that it is normalized and can be used for cross-comparisons among different models and quantities, regardless of units. The value of *IA* varies between 0 and 1, a value of 0 indicates complete disagreement between the model prediction and observations, and 1 indicates perfect agreement.

Figures 5a, 5d, 6a, and 6d show the comparison of free surface elevation (WG1) and flow velocity (ADV2) for Cases I and II respectively at the most offshore location. *IA*s for WG1 and ADV2 in both cases are greater than 0.9 which confirms that the numerical wave generation is appropriate. Figures 5b, 5e, 6b, and 6e show the results (WG12, ADV10) in the surf zone. Even with the occurrence of wave breaking, *IA*s for WG12 and ADV10 in both cases still remain at approximately 0.85 showing the model's capability of resolving complex wave breaking processes. Figures 5c and 5f show the result (WG14, ADVP1) of Case I located in the swash zone, whereas Figures 6c and 6f show the results (WG14, ADVP1) of Case II located in between the inner surf and swash zones.

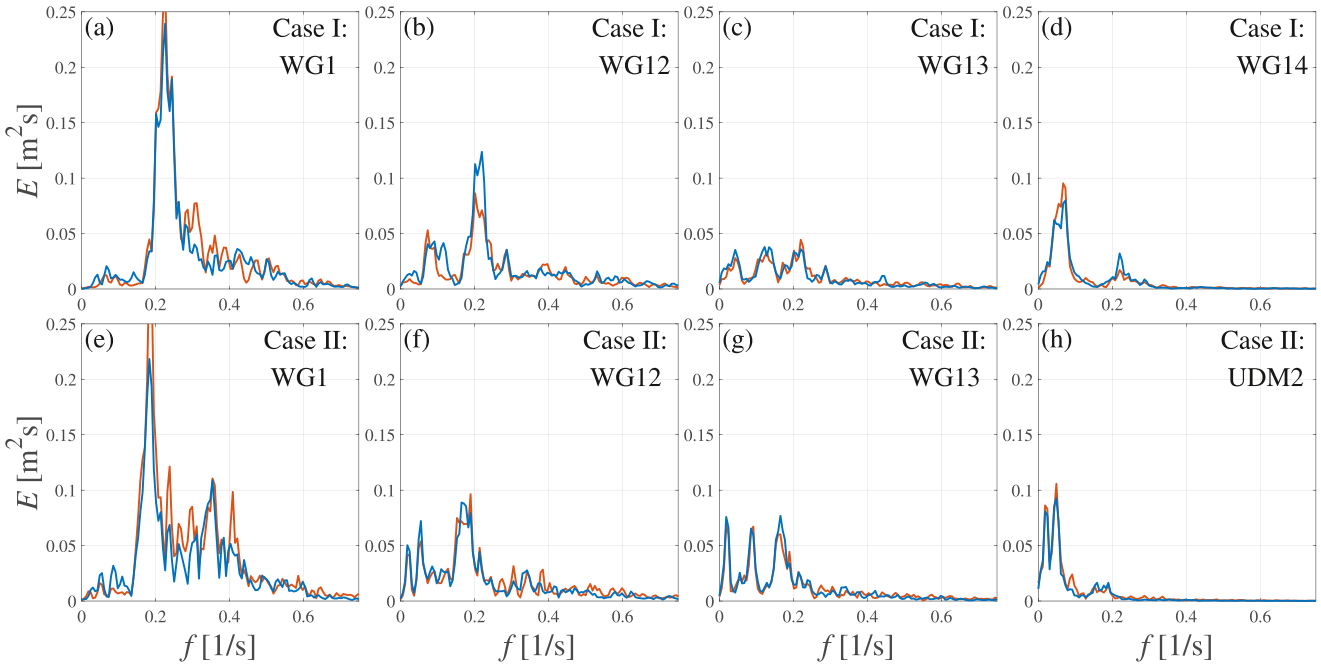

Figure 7. Wave spectra comparison between model results (blue lines) and observations (orange lines). (a)–(d) are the results of Case I and (e)–(h) are of Case II. Columns from left to right denote WG1, WG12, WG13, and WG14 (UDM2 for Case II).

The surface elevation change for WG14 is smaller than those in the offshore locations, and the overall wave period increases, demonstrating the incident waves have transformed from sea-swell dominant waves to more infragravity dominant waves. The model results of WG14 for both cases agree with measured data with *IA*s at approximately 0.85. It should be emphasized that the velocity measurement (ADPV1) was taken very close to the bed (26 mm above the bed for Case I and 5 mm above the bed for Case II) and located in the wet-dry area, which is extremely challenging for numerical models to match, but the *IA*s for both cases remain 0.73 and 0.81 for Cases I and II, respectively. It is worth pointing out that some experimental data time series contain gaps when the water level dropped below the sensor elevation. Other time gaps arise through quality control procedures that remove noise caused by air bubbles, especially in the swash zone.

The irregular waves lead to the varying wave breaking point and form infragravity waves (Symonds et al., 1982). This causes a time-varying radiation stress which is balanced by a time-varying wave setup and partially transfers energy from sea-swell frequencies (typical periods of 2–20 s) to infragravity frequencies (typical periods of 25–250 s). Wave energy shifting from the sea-swell band to infragravity band along the cross-shore direction can be observed in the physical experiment and numerical simulations (Figure 7). The peak frequency on the offshore side before wave breaking is approximately 0.2 Hz for both cases, which is consistent with the specified peak wave period T_p of each case. Waves start breaking when reaching the surf zone, and the wave energy at peak frequency decreases indicating significant dissipation (Figures 7b and 7f). The intensity of wave spectral energy becomes even lower when reaching the inner surf zone (Figures 7c and 7g) due to more dissipation. Importantly, once waves propagate close to the shoreline, the energy at sea-swell frequencies decreases by almost an order of magnitude and infragravity frequencies have become dominant (Figures 7d and 7h). These important features of wave energy dissipation and shifting to low wave frequency are captured well by the numerical model.

Higher-order wave statistics and undertow currents are key parameters in modeling onshore and offshore sediment transport (Rafati et al., 2021; Roelvink et al., 2009). Wave-averaged quantities, including mean water level (*MWL*), root-mean-square wave height (H_{rms}), wave skewness (*Sk*) and asymmetry (*As*), and offshore-directed mean currents (undertow) are investigated. The mean water level is the time-averaged free surface elevation (η) and the spectral root-mean-square wave height is defined as

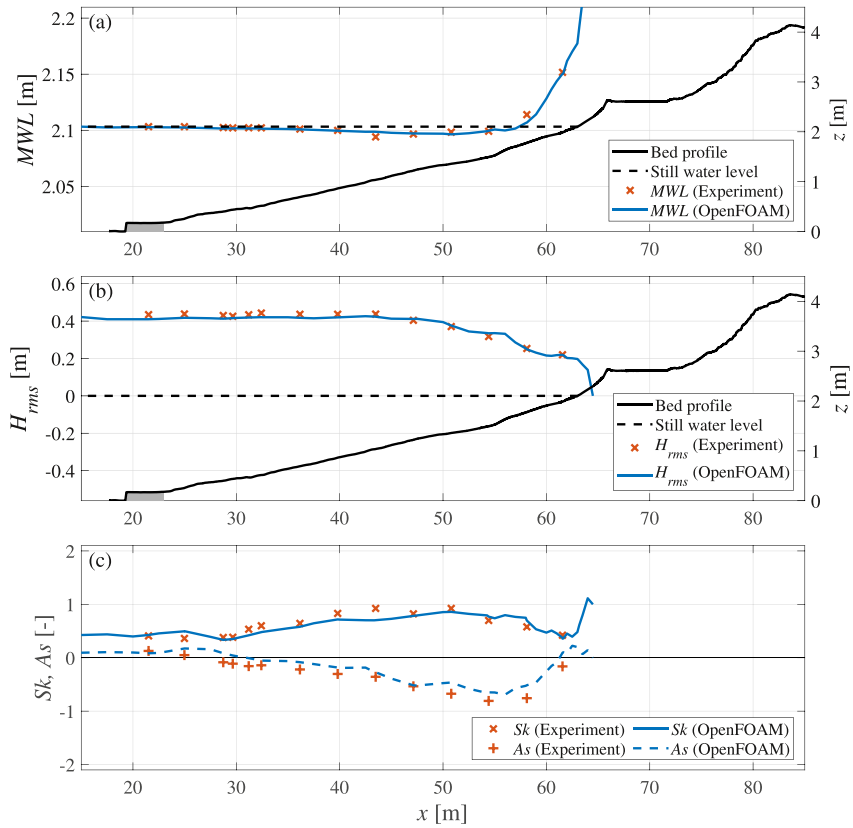

Figure 8. A comparison of (a) mean water level (*MWL*), (b) root-mean-square wave height (H_{rms}), and (c) wave skewness (*Sk*) and asymmetry (*As*) for Case I between simulation results (lines) and measured data (symbols).

$$H_{rms} = \sqrt{8 \int E(f)\, df} \tag{8}$$

where E is the wave energy density of a wave spectrum. Wave skewness and asymmetry are the third-moment quantities that can be applied to the wave motion of either free surface elevation or orbital velocity. In this study, wave skewness and asymmetry were calculated using free surface elevation because of the availability of a large number of wave gauge data from the physical experiment. They are calculated as (Elgar & Guza, 1985),

$$Sk = \frac{\overline{\eta^3}}{\overline{\eta^2}^{\frac{3}{2}}} \tag{9}$$

$$As = \frac{\overline{\mathcal{H}(\eta)^3}}{\overline{\eta^2}^{\frac{3}{2}}} \tag{10}$$

where $\bar{\cdot}$ is the time-average operator and $\mathcal{H}(\cdot)$ denotes Hilbert transform of the time series.

The overall comparison between the model and experimental results shows a good agreement in both Cases I (Figure 8) and II (Figure 9). The difference between the modeled and measured *MWL* is within 2 cm (one cell thickness) and it can be concluded that wave set-up and set-down are well-predicted by the model (Figures 8a and 9a). The agreement for the cross-shore H_{rms} for both cases is also good (Figures 8b and 9b). H_{rms} slightly increases due to the shoaling process before wave breaking. Since there is no sandbar present in Case I and waves break closer to the shoreline, the breaker point is located at approximately $x \approx 50$ m. A sandbar is formed in Case II, and waves break at $x \approx 45$ m, slightly landward of the sandbar crest. Due to the presence of a berm, the beach slope is

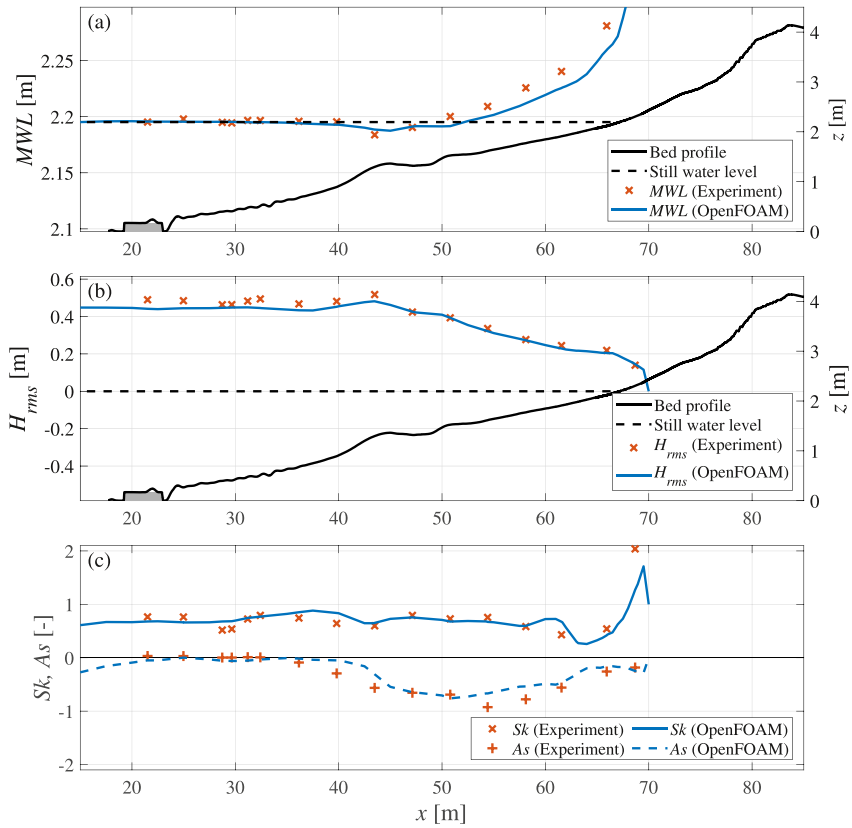

Figure 9. A comparison of (a) mean water level (*MWL*), (b) root-mean-square wave height (H_{rms}), and (c) wave skewness (*Sk*) and asymmetry (*As*) for Case II between simulation results (lines) and measured data (symbols).

steeper in Case I compared to Case II. The steeper beach slope in Case I corresponds to a sharper decrease in H_{rms} whereas the milder beach slope (due to the absence of a berm) in Case II shows a more gradual decrease in wave height.

When waves propagate toward the shoreline, wave non-linearity becomes apparent. The wave skewness of Case I shows a gradual increase from approximately 0.4 to 0.9 before reaching the breaker point at $x \approx 50$ m (Figure 8c), and landward of the wave breaking point, it drops back to 0.4. With a larger offshore wave height, the wave skewness of Case II maintains at approximately 0.7 (Figure 9c). There is a small decrease in wave skewness just before the wave breaking point ($x \approx 45$ m) but it soon recovers to 0.7. The wave skewness drops to 0.4 landward of $x \approx 55$ m. In Case I, wave asymmetry gradually reaches −0.8 until 5 m landward of the breaker point, and then sharply returns back to 0 at the shoreline. In Case II, wave asymmetry remains 0 until waves approach the sand bar where asymmetry rapidly approaches −0.7. This value is maintained for 5–10 m landward of the sand bar crest, and then gradually returns back to 0 at the shoreline.

The offshore-directed mean current, namely undertow, cannot be directly resolved by depth-integrated and/or time-averaged models since it is related to wave-breaking driven turbulence and its inhomogeneous distribution in the water column. With LES, these complex interactions can be resolved, and so does the undertow profile after taking the time average of flow velocity. The undertow profiles for Cases I and II are shown in Figures 10a and 10b. The upper part of the water column shows onshore-directed mean velocity which is caused by the Stokes drift and wave breaking. The presence of undertow balances with the onshore flow and its magnitude becomes larger when wave breaking is more intense. The depth-averaged mean current can be calculated by averaging the flow velocity of the lower part of the water column (Figure 10c). The comparisons between the model results and measured data show good agreement.

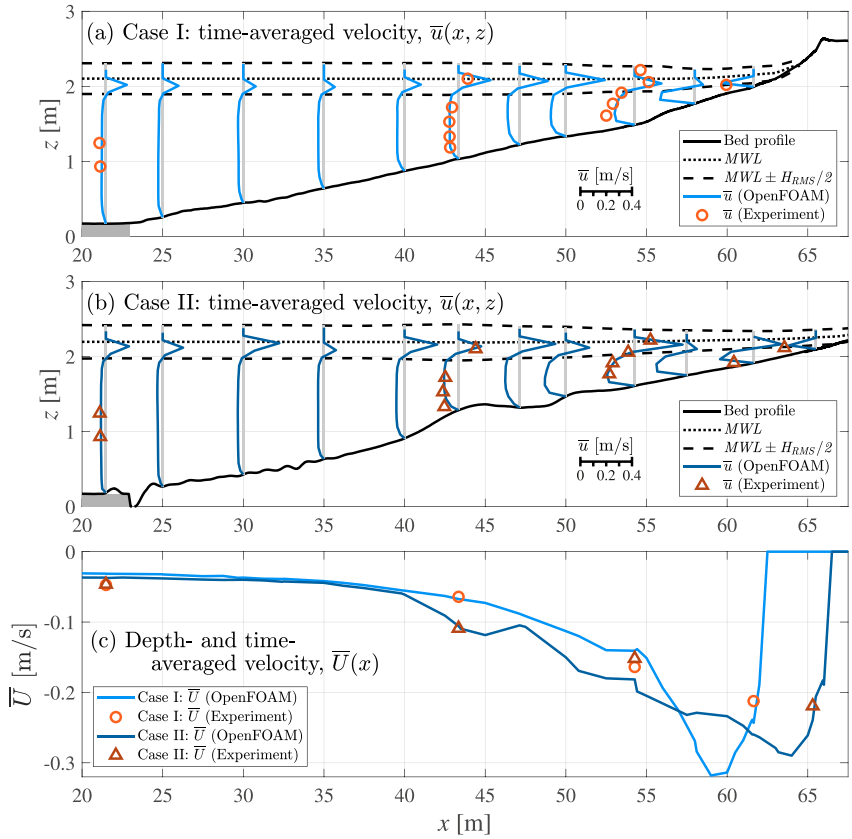

Figure 10. Undertow profiles along the cross-shore direction for (a) Case I and (b) Case II. (c) Depth-averaged undertow velocity for Cases I and II. Lines denote simulation data and symbols denote measured data.

4. Results

In the following sections, several quantities including the Q-criterion, Shields parameter (θ), Sleath parameter (S), and turbulent kinetic energy (TKE) are to analyze the simulation data. TCS are identified using the Q-criterion method (Hunt et al., 1988), which is calculated based on the local velocity gradient tensor:

$$Q = \frac{1}{2}\left[\left(\frac{\partial u_k}{\partial x_k}\right)^2 - \left(\frac{\partial u_i}{\partial x_j}\frac{\partial u_j}{\partial x_i}\right)\right]. \tag{11}$$

Generally, a higher Q value correlates with a higher turbulent intensity.

The Shields parameter (θ) is a common nondimensional measure of bottom shear stress (τ_w) that strongly correlates with sediment transport and it is written as

$$\theta = \frac{\tau_w}{\rho(s-1)\,gd}. \tag{12}$$

Previous research has demonstrated that the horizontal pressure gradient plays a crucial role in driving momentary bed failure (or called plug flow), particularly at the front of bores or breaking waves (Foster et al., 2006; Sleath, 1999). The Sleath parameter (S), defined as the ratio of the horizontal pressure-induced disruptive force at the bed to the stabilizing force of particles due to gravity, is a useful measure for the occurrence of momentary bed failure and it is written as

$$S = \frac{-\partial p/\partial x}{\rho(s-1)\,g} \tag{13}$$

Laboratory observations (Sleath, 1999) suggest that the Sleath parameter exceeding a critical value of 0.29 may trigger momentary bed failure while field observations indicate 0.1 (Foster et al., 2006).

In addition to Shields and Sleath parameters, a significant effect of TKE on sediment transport in the inner surf and swash zones has also been demonstrated (Butt et al., 2004). In this study, TKE is calculated through spanwise averaging (Kim et al., 2017; Zhou et al., 2014) over the resolved velocity field which can be written as

$$k = \frac{1}{2}\langle u_i' u_i' \rangle \tag{14}$$

in which $u_i' = u_i - \langle u_i \rangle$ is the fluctuation of the flow velocity; $\langle \cdot \rangle$ is the spanwise average operator over the resolved field.

4.1. Case I: Berm Erosion Stage

In Case I (trial no. 5), the breaker type is classified as a spilling breaker according to Battjes (1974) and waves tend to break closer to the foreshore due to the absence of a sandbar. As shown in Figure 8b, the root-mean-square wave height starts to decrease gradually at $x \approx 50$ m, signaling the commencement of the surf zone. A more significant drop is then observed in the inner surf zone at $x \approx 55$ m. Intense wave breaking and dissipation occur at $x \approx 55$ m, which is only about 7 m from the shoreline, and the flow depth is less than 0.5 m. Consequently, breaking waves are likely to directly interact with the backwash flows and the seabed.

Due to a much shorter distance between the breaker line and the outer swash zone in Case I, larger waves tend to break closer to the shoreline, colliding with the preceding backwash. It is important to note that the geometry of the berm front is not a constant slope (linear profile); rather, it exhibits a curvature that becomes steeper close to the berm top. The slope is approximately 0.14 at the berm foot, increasing to around 0.2 at the central part of the berm and increasing further to almost 0.5 at the top part of the berm. Runup appears to be constrained by the large slope of the berm front, with most runup events being lower than the berm height; only occasional large swash events result in overwash of the berm. The swash zone is only about 4 m long in cross-shore extent. More than 10 swash events were examined, and two consecutive swash events representing Case I are selected for analysis. The leading event occurring between $t = 270.0$–273.0 s (Figure 11a) is characterized by a strong incoming wave that generates a near-bed velocity of 2.5 m/s, contrasting with the backwash flow of -1.5 m/s at the location $x = 61.64$ m of ADPV1 (Figure 11b). Conversely, the subsequent event between $t = 276.0$–279.0 s (Figure 15a) is dominated by backwash, where under the passage of the incoming wave, a near-zero near-bed velocity against the backwash flow of intensity exceeding -1 m/s (Figure 15b) was observed.

4.1.1. Strong Wave-Backwash Interaction Event in Case I

The swash event commences with a strong backwash flow from the preceding swash with a high Shields parameter exceeding 4 ($x \approx 63.5$m in Figure 11c), followed by a large incoming wave (Figures 11e and 11f). As the wave shoals, it collides with the backwash flow, exhibiting comparable Shields parameters of approximately 2 on both sides of the wavefront, albeit with opposing directions (onshore and offshore) ($x \approx 58.5$ m in Figure 11e). Importantly, the Sleath parameter beneath the breaking wavefront surpasses 0.1 (Figure 11f), indicative of the potential for momentary bed failure. Crescent-shaped TCS distributed in the spanwise direction are observed as the spilling breaker evolves and continues to propagate onshore ($x \approx 61$ m in Figures 11g and 11h). A large and variable Shields parameter distribution, with magnitudes fluctuating between 0 and 7, aligns with the TCS (Figure 11g). High Sleath parameters of approximately 0.5, forming stripe-like patterns oriented in the spanwise direction, are observed at the breaking-wave front (Figure 11h). As the TCS vanish during uprush and the flow depth becomes shallow (Figures 11i and 11j), the Shields parameter increases dramatically (Figure 11i). Behind the uprush front, a finger-shaped pattern emerges (Kim et al., 2017), orienting itself in the streamwise direction.

By applying spanwise averaging, the cross-shore distributions of the mean Shields and Sleath parameters, as well as their standard deviations (quantifies the spanwise variability due to 3D flow instabilities and turbulence), are examined more quantitatively (Figure 12). Incoming breaking waves typically result in positive Shields and Sleath parameters, due to the onshore wave-induced velocity and surface elevation difference at the front (Figures 12a and 12b). Positive Shields parameters at the wavefront are observed ($x \approx 55.5$ m in Figure 12a and $x \approx 58$ m in Figure 12b) in the simulation. Meanwhile, the negative Shields parameter caused by backwash is

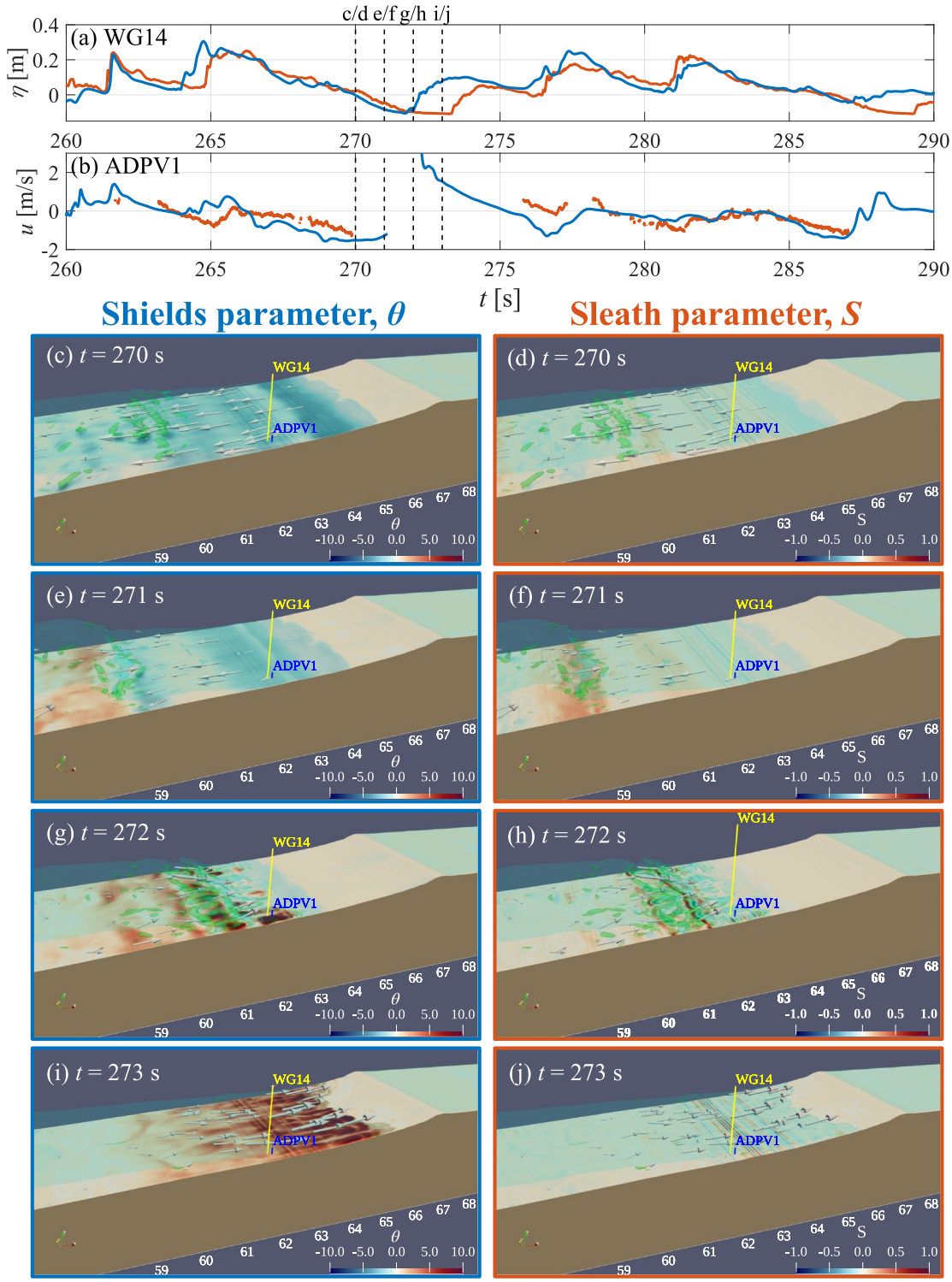

Figure 11. Time series of (a) free surface elevation and (b) streamwise flow velocity for a 30-s interval of Case I. The blue and orange lines denote numerical simulation and measured results, respectively. (c)–(j) Show the snapshots of the inner surf and swash zones at (c)–(d) t = 270.0 s, (e)–(f) t = 271.0 s, (g)–(h) t = 272.0 s, and (i)–(j) t = 273.0 s. The contour plots at the bed shows the Shields (c, e, g, i) and Sleath (d, f, h, j) parameters. The transparent cyan isosurface denotes free surface and the transparent green isosurface shows the turbulent coherent structures with a Q-criterion of 25.

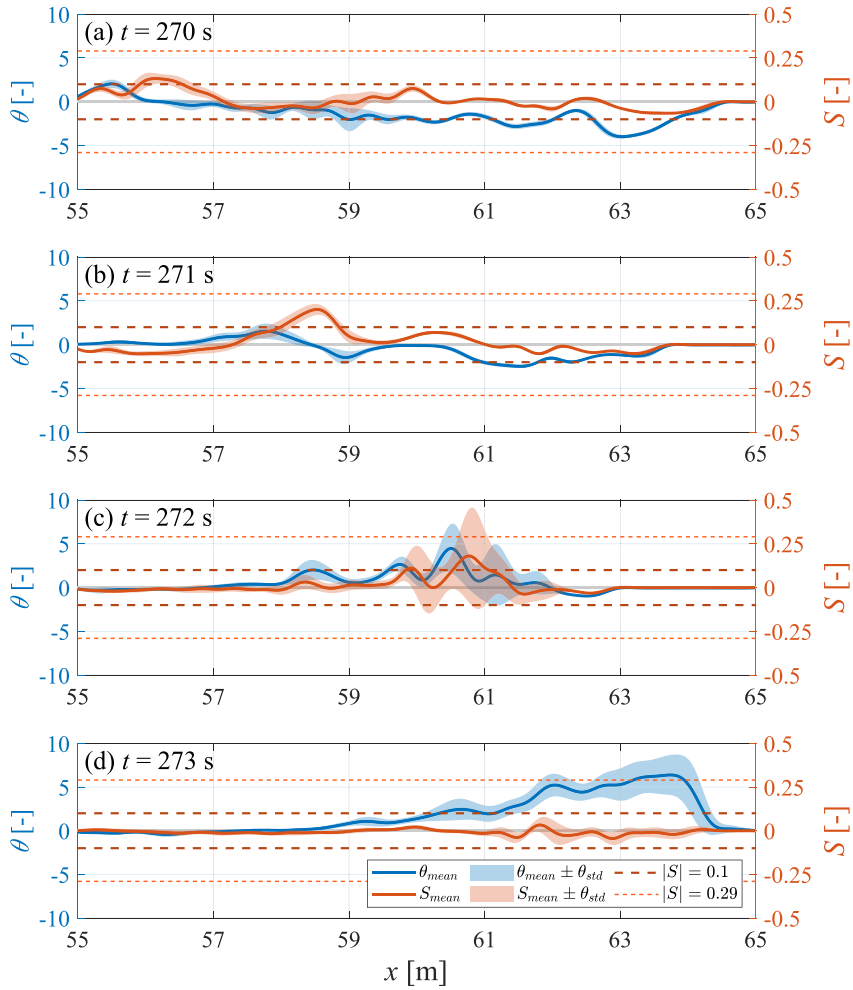

Figure 12. Cross-shore distribution of Shields parameter (blue) and Sleath parameters (orange) for Case I at (a) t = 270.0 s, (b) t = 271.0 s, (c) t = 272.0 s, and (d) t = 273.0 s. Solid lines and lighter color patches denote the spanwise averaged quantities and plus/minus one standard deviation.

observed on the landward side of the wavefront ($x > 58.5$ m in Figures 12a and 12b). Notably, when the incoming wave begins to collide with the backwash (Figure 12b), the Sleath parameter exceeds the critical value of 0.1 between $x \approx 58$ - 59 m, implying that momentary bed failures may occur during the encounter. Subsequently, the incoming wave strongly interacts with the backwash and causes chaotic flow motion. The collision of the two leads to a drastic increase of the spanwise variation of both Shields and Sleath parameters ($x \approx 60$–62 m in Figure 12c). The fluctuation of the Sleath parameter is particularly notable, with $x \approx 60$–61.5 m exceeding 0.1 and $x \approx 60.5$–61 m even exceeding the more conservative critical value of 0.29, indicating that momentary bed failure significantly occurs across an extensive area. The strong incoming wave soon overcomes the backwash flow, and the mean Shields parameter becomes fully positive while the Sleath parameter calms to nearly zero. The bore then uprushes onto the berm front, causing a large Shields parameter (mean value of approximately 5, combined with the fluctuation reaching over 8), which can substantially erode the berm (Figure 12d), while the Sleath parameter plays a minor role.

The vertical profiles of the spanwise-averaged velocity and the vorticity at the inner surf/swash transition zone are shown in Figure 13. The backwash flow, exceeding 1 m/s, moves toward the offshore direction (Figure 13a). Concurrently, the incoming wave encounters the backwash flow (Figure 13b). The maximum flow velocity of the incoming wave, reaching approximately 2.0 m/s at the breaking front atop the water column, overpowers the backwash flow. During their collision, a thin layer of positive vorticity appears at the bed and flow separation

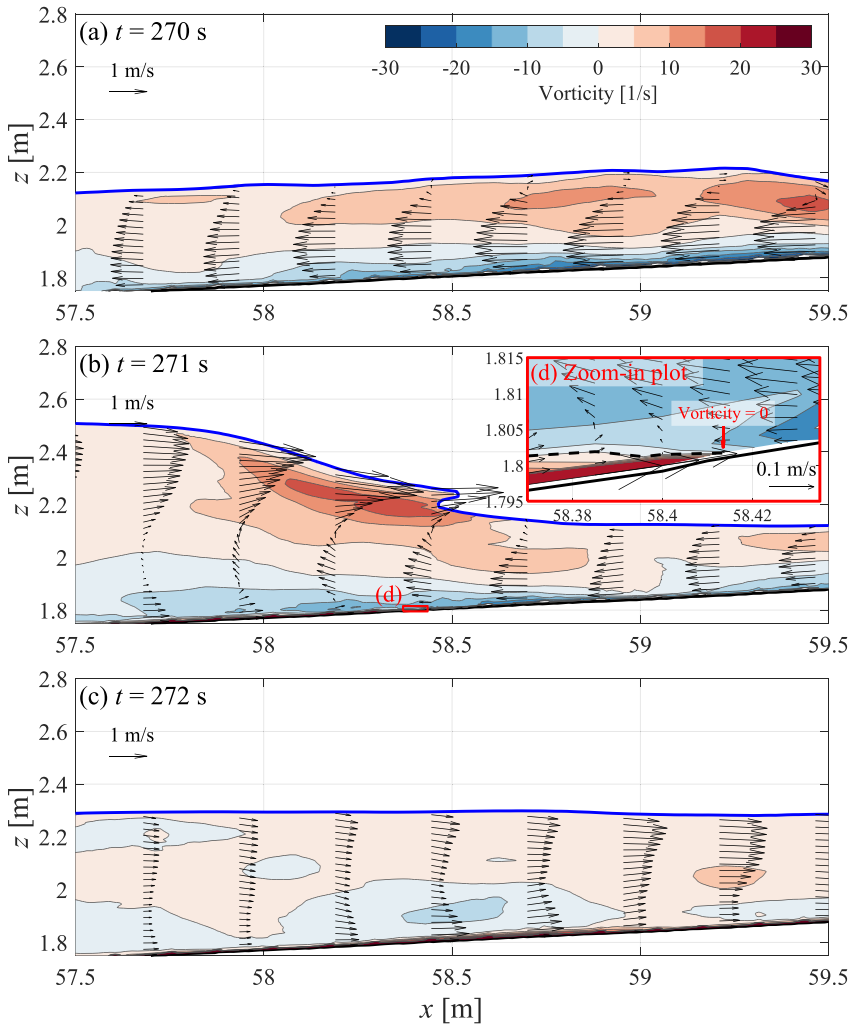

Figure 13. Spanwise averaged cross-shore velocity profiles for Case I at (a) t = 270.0 s, (b, d) t = 271.0 s, and (c) t = 272.0 s.

occurs for the backwash flow, detaching it from the bed (Figure 13d). The flow separation point can be identified at the location where vorticity changes its sign (Sou & Yeh, 2011), which is located at $x \approx 58.4$ m. Due to the flow separation, the backwash flow injects into the water column, nullifying the onshore velocity but the velocity only becomes offshore directed in the middle of the water column. Despite the presence of backwash, the incoming wave eventually overcomes the backwash flow (Figure 13c). The formation of boundary layer separation during swash-wave interaction has been observed in previous laboratory studies (Sou & Yeh, 2011; Sumer et al., 2013) and it may have a large effect on sediment transport. The regime of flow separation between x = 58–59 m coincides with the location of high Sleath parameter values (Figure 12b).

Because of the absence of the sand bar, waves break closer to the beachfront in Case I which leads to more intense interaction between incoming waves and the backwash and hence direct turbulence-bed interaction (Figure 14). As the incoming wave breaks as a spilling breaker, results show that the location of the high TKE area coincides with the TCS (Figures 11e and 14a) and the TKE level is around 0.4 m^2/s^2 in the core of the breaker. As the breaking wave evolves toward a bore, the highly turbulent front impinges onto the bed. TKE level around the impingement point is even larger than that in the spilling breaker and almost reaches 0.5 m^2/s^2 (Figure 14b). The TKE soon gets dissipated when the bore rushes up to the berm due to the deceleration and friction (Figure 14c).

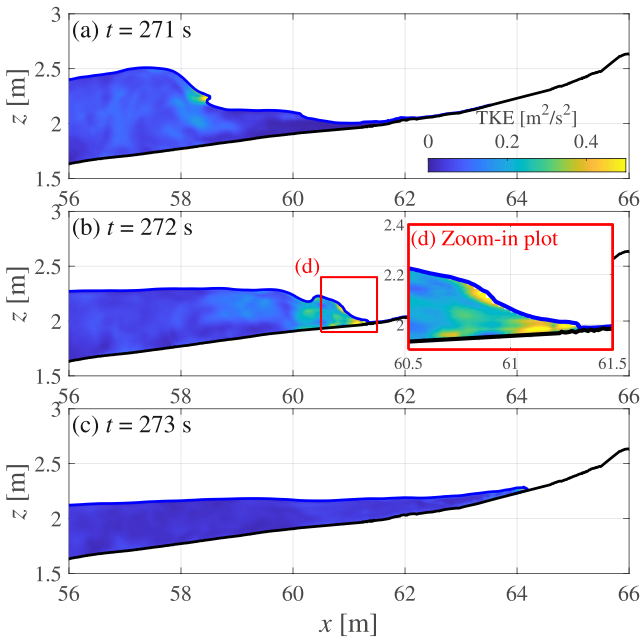

Figure 14. Turbulent kinetic energy in the swash zone for Case I at (a) t = 271.0 s, (b, d) t = 272.0 s, and (c) t = 273.0 s, respectively.

4.1.2. Backwash-Dominated Swash Event in Case I

After the previous uprush, the flow direction reverses and backwash follows (Figure 15c). During this backwash phase, the Shields parameter is constrained to a magnitude of approximately 2–4 which is smaller but comparable to the backwash of the previous event (compare to Figure 12c). The subsequent incoming wave, on the other hand, is notably weaker compared to the backwash flow (Figure 15b) and the backwash flow almost impedes the incoming wave propagation (Figures 15e and 15g). The incoming wave shortly evolves into a weak uprush (Figures 15i and 15j) with a Shields parameter of approximately 2, markedly lower than the previous uprush (Figure 11i). Although not as pronounced as in the previous event, a finger-shaped pattern is discernible here. TCS are primarily observed during the collision between the incoming wave and backwash (Figures 15e and 15f). The region with a higher Sleath parameter is associated with the incoming wave, however, the overall magnitude is lower than 0.29.

In this backwash-dominated event, the incoming wave is weak and a small positive Shields parameter is observed during the wave passage (Figure 16a, at $x \approx$ 56–59 m). Instead, the negative Shields parameter, induced by the backwash flow, is more pronounced ($x >$ 61.5 m). The Sleath parameter at the breaking wavefront attains a value of 0.1, falling below the conservative critical threshold of 0.29 (Figures 16b and 16c). In contrast to the previous strong wave-backwash event, the spanwise variability of the Sleath parameter in this case is negligible (Figure 16c). The Sleath parameter soon diminishes to nearly zero, while the negative Shields parameter (indicative of backwash flow) transitions to a positive value, signifying uprush (Figure 16d). At the uprush tip, the Shields parameter is nearly 2, and the standard deviation is about 1, both of which are considerably smaller than those in the strong wave-backwash event.

From the spanwise-averaged velocity profiles in the cross-shore direction (Figure 17), the backwash flow exceeds 1 m/s, a magnitude similar to that in the preceding event (Figure 17a). Given that the backwash flow is significantly stronger than the incoming wave, a weaker flow separation is observed (Figure 17b). The near-bed vorticity changes sign at x = 62.4 m. The corresponding Sleath parameter is about 0.17 (Figure 16c), which is smaller than that observed in the strong interaction event. Eventually, the weak bore overtakes the backwash (Figure 17c), resulting in a shift in the velocity toward a positive direction. Comparing with results shown in Section 4.1.1, strong backwash flow separation and large Sleath parameter require a relatively balanced intensity between incoming wave and backwash flow.

4.2. Case II: Bar Formation Stage

For Case II (trial no. 20), due to the earlier berm erosion that occurred during trials no. 1–13, the sediment from the berm had already been transported offshore and formed a sandbar at $x \approx$ 45 m (Figure 2b). Waves shoal on the seaward side of the bar and break on the landward side. The sandbar results in waves breaking farther offshore compared to Case I. The distance between the wave breaking point and the shoreline is about 20 m while the flow depth at the breaking point is about 0.8 m. These two quantities are greater than those in Case I. As the breaking waves enter the surf zone in Case II, the breaking wave has transformed into a weaker bore and hence the interaction between the bore-generated turbulence and the bed is weaker than Case I. This main difference causes distinct inner surf and swash zone features between Cases I and II.

The foreshore slope in Case II is approximately 0.09, which is milder than the slope of the berm front in Case I. As a result, the cross-shore length of the swash zone in Case II spans roughly 8 m, nearly double that of Case I. Moreover, in contrast to Case I, where breaking waves tend to directly interact with the backwash, it is the bores that interact with the backwash in Case II. These factors cause longer-duration and more isolated uprush and backwash events. More than 10 swash events were examined in Case II, and two representative swash events (t = 477.0–480.0 s and t = 484.0–487.0 s) are selected for analysis.

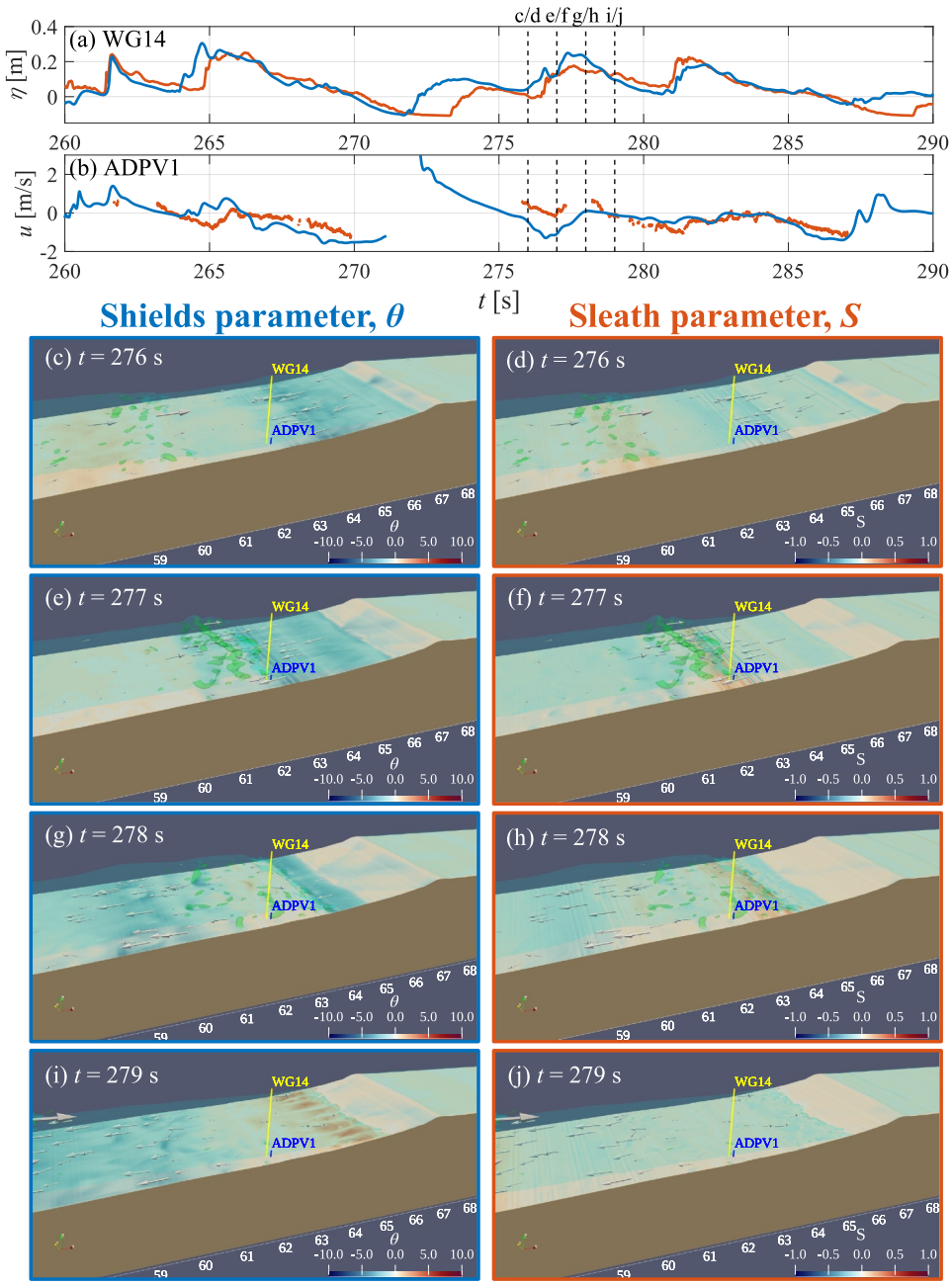

Figure 15. Time series of (a) free surface elevation and (b) streamwise flow velocity for a 30-s interval of Case I. The blue and orange lines denote numerical simulation and measured results, respectively. (c)–(j) Show the snapshots of the inner surf and swash zones at (c)–(d) t = 276.0 s, (e)–(f) t = 277.0 s, (g)–(h) t = 278.0 s, and (i)–(j) t = 279.0 s. The contour plot at the bed shows the Shields (c, e, g, i) and Sleath (d, f, h, j) parameters. The transparent cyan isosurface denotes free surface and the transparent green isosurface shows the turbulent coherent structures with a Q-criterion of 25.

4.2.1. Bore-Dominated Swash Event in Case II

In this event, the backwash is relatively weak (Figure 18c, Shields parameter is around 1), while the strong incoming bore induces a Shields parameter greater than 2. Initially, the TCS are mainly aligned parallel to the wavefront (Figures 18c and 18d). As the bore propagates toward the shoreline, these TCS gradually orient themselves in the streamwise direction (Figures 18e and 18f). The distribution of the Sleath parameter and Shields parameter are more chaotic but seem to correlate with the TCS. In certain locations, the Shields parameter reaches

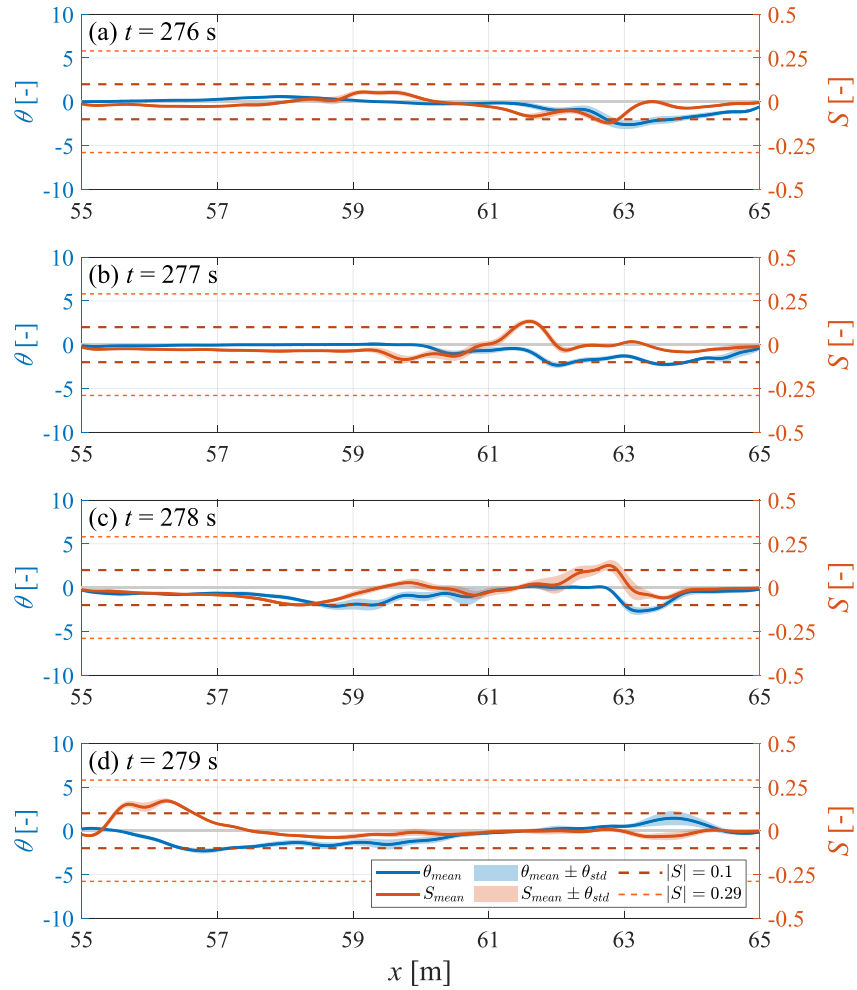

Figure 16. Cross-shore distribution of Shields parameter (blue) and Sleath parameters (orange) for Case I at (a) t = 276.0 s, (b) t = 277.0 s, (c) t = 278.0 s, and (d) t = 279.0 s. Solid lines and lighter color patches denote the spanwise averaged quantities and plus/minus one standard deviation.

an approximate magnitude of 4, while in others, it remains low. This indicates that in Case II the incoming wave approaching the swash is generally weaker than that in Case I, and therefore, the overall intensities of the Shields and Sleath parameters are lower but populated with locally higher intensity spots associated with TCS. As the bore enters the swash zone and rushes up the foreshore, TCS dissipate, and a finger-shaped pattern of high Shields parameter begins to emerge (Figures 18g and 18i). This pattern fully develops and intensifies as the runup continues to travel in the onshore direction. However, the Sleath parameter disperses during uprush (Figures 18h and 18j).

Generally, the Shields parameter in this event is relatively small within the inner surf zone (Figures 19a and 19b, $x \approx 62 - 66$ m). It is not until the bore travels into the swash zone that large spanwise variabilities and larger magnitude of Shields parameter start to emerge due to interaction with the bed in shallow water (Figures 19c and 19d). During the uprush, the spanwise-averaged Shields parameter initially increases to a magnitude of approximately 2 with high spanwise variation (Figure 19c), and then it further increases to nearly 5 as the bore moves farther onshore (Figure 19d), which is marginally lower than the strong wave-backwash interaction event in Case I (Figure 12d). On the other hand, the Sleath parameter during bore propagation (Figures 19b and 19c), is much smaller than that in Case I. The maximum spanwise-averaged Sleath parameter approaches approximately 0.1 but falls short of the conservative threshold value of 0.29.

While the backwash flow in this event is weak (approximately −0.2 m/s, Figure 20a), the incoming bore possesses a large flow velocity of 1.5 m/s. When the incoming bore encounters the backwash (Figure 20b), it

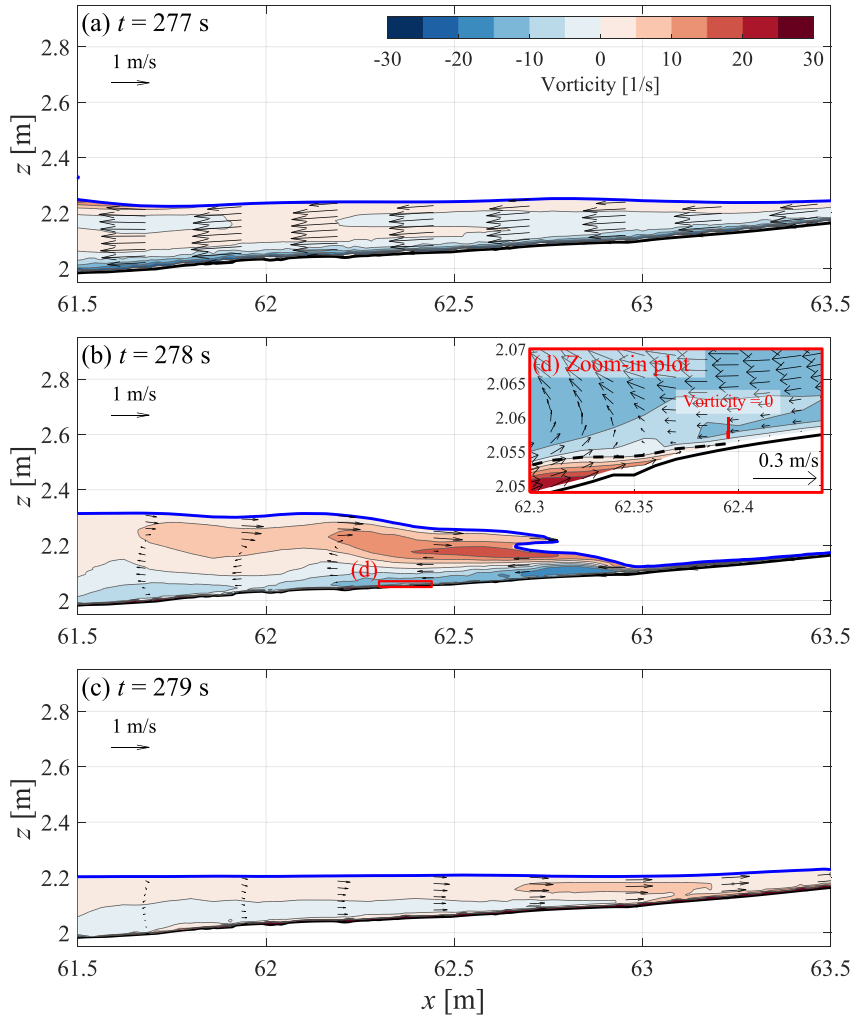

Figure 17. Spanwise averaged cross-shore velocity profiles for Case I at (a) t = 277.0 s, (b, d) t = 278.0 s, and (c) t = 279.0 s.

completely overtakes the backwash flow (Figure 20c). Nevertheless, the incoming bore is of weaker intensity and water level compared to the incoming breaking wave observed in the strong interaction event in Case I. As a result, no distinct interaction between the bore and backwash is observed, not to mention flow separation. The weak backwash flow and the lack of strong interaction between the bore and the backwash flow leads to a much lower Sleath parameter. Although the Shields parameter is generally lower than that in Case I, large Shields parameter during uprush (Figures 19c and 19d) with pronounced spanwise variability is a common feature in the upper swash.

Similar to Case I, breaking waves and bores dominate the generation of TKE in this event. However, the main difference is that the high TKE area in this event is not adjacent to the bed (Figure 21a). The maximum TKE level during the bore passage is approximately 0.4 m^2/s^2 which is slightly less than Case I. The TKE dissipates significantly before reaching the swash zone and the TKE near the bed is small (Figures 21b and 21c).

4.2.2. Backwash-Dominated Swash Event in Case II

In the ensuing swash event (Figure 22), the bore is comparatively weaker than the prior Case II bore (Figure 18). The transition period from uprush to backwash is longer than in Case I owing to the greater length of the swash zone. The extended duration allows the backwash flow to accelerate, resulting in a high Shields parameter with a magnitude of approximately 5 during the backwash (Figures 22e, 22g, and 22i) while the location of the peak

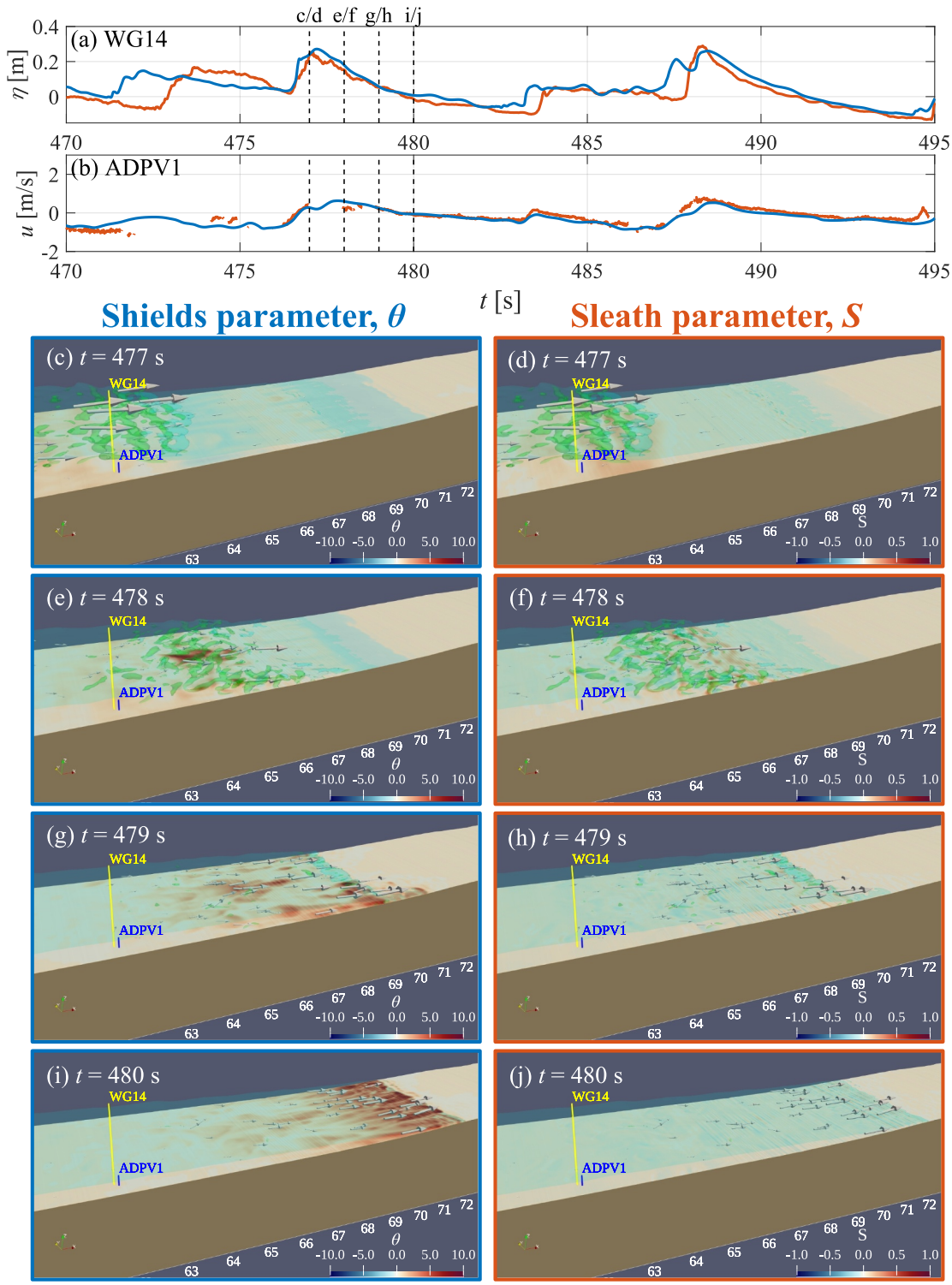

Figure 18. Time series of (a) free surface elevation and (b) streamwise flow velocity for a 30-s interval of Case II. The blue and orange lines denote numerical simulation and measured results, respectively. (c)–(j) Show the snapshots of the inner surf and swash zones at (c)–(d) t = 477.0 s, (e)–(f) t = 478.0 s, (g)–(h) t = 479.0 s, and (i)–(j) t = 480.0 s. The contour plot at the bed shows the Shields (c, e, g, i) and Sleath (d, f, h, j) parameters. The transparent cyan isosurface denotes free surface and the transparent green isosurface shows the turbulent coherent structures with a Q-criterion of 25.

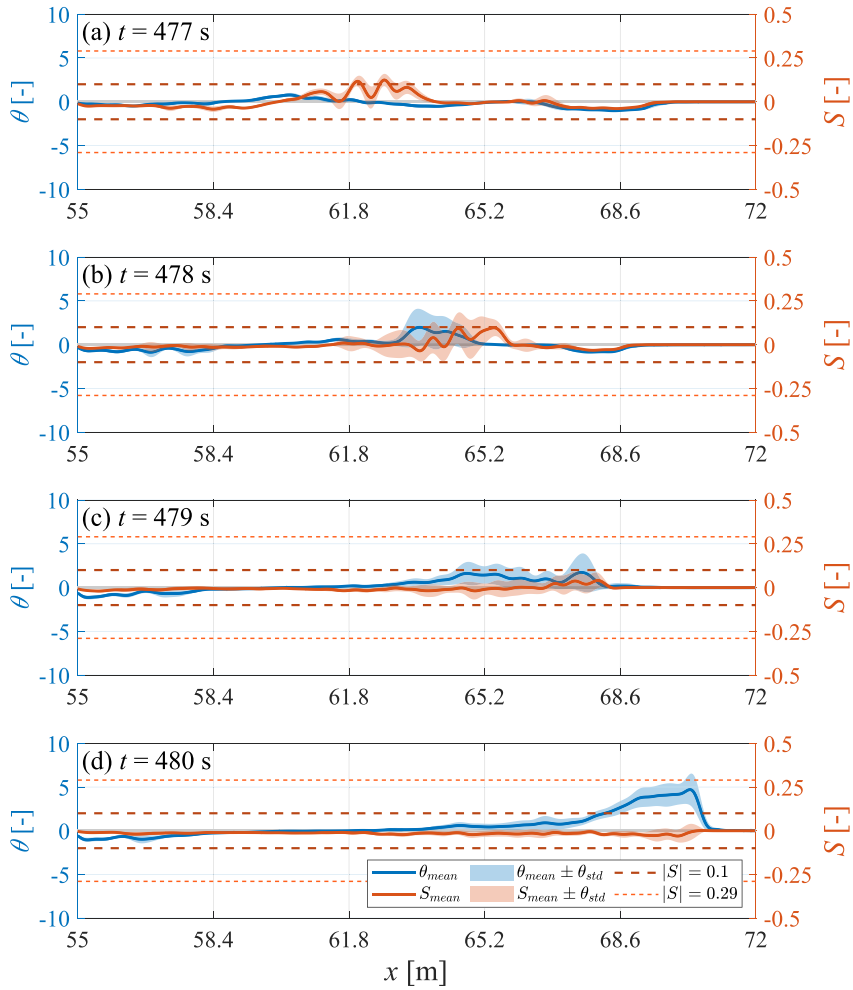

Figure 19. Cross-shore distribution of Shields parameter (blue) and Sleath parameter (orange) for Case II at (a) t = 477.0 s, (b) t = 478.0 s, (c) t = 479.0 s, and (d) t = 480.0 s. Blue and orange colors denote Shields and Sleath parameters, respectively. Solid lines and lighter color patches denote the spanwise averaged quantities and plus/minus one standard deviation, respectively.

value progressively shifts offshore. This magnitude is slightly greater than that observed in the backwash-dominated event in Case I (Figure 16). The Shields parameter consistently remains negative given the weak nature of the incoming bore. The Sleath parameter is minimal throughout this swash event (Figures 22d, 22f, 22h, and 22j). Both the Shields and Sleath parameters exhibit high uniformity in the spanwise direction (Figure 22). Only a scant amount of TCS emerge when the incoming bore collides with the backwash flow (Figures 22e and 22f), and these structures rapidly disperse thereafter (Figures 22g and 22h). In this particular swash event, the bore fails to overcome the backwash flow, and consequently, no subsequent uprush is observed following the bore (Figures 22g, 22i, 23b, and 23c).

The velocity of the backwash flow gradually increases from approximately 0.3 m/s (Figure 23a) to 1 m/s (Figure 23b), subsequently colliding with the incoming bore at $x \approx 63.1$ m (Figure 23b). Being stronger than the incoming bore, the backwash flow is able to overcome the positive velocity driven by the bore and velocity in the lower part of the water column is negative, indicative of offshore flow (Figure 23b). However, no flow separation is observed. As the backwash flow continues to accelerate, it eventually surpasses the incoming bore, causing the entire flow field to ultimately shift in the offshore direction (Figure 23c).

The lack of strong interaction between the incoming waves and backwash flow generates weak spanwise variability and small Sleath parameter. In this event, the incoming bore is also weak and hence the entire event is dominated by

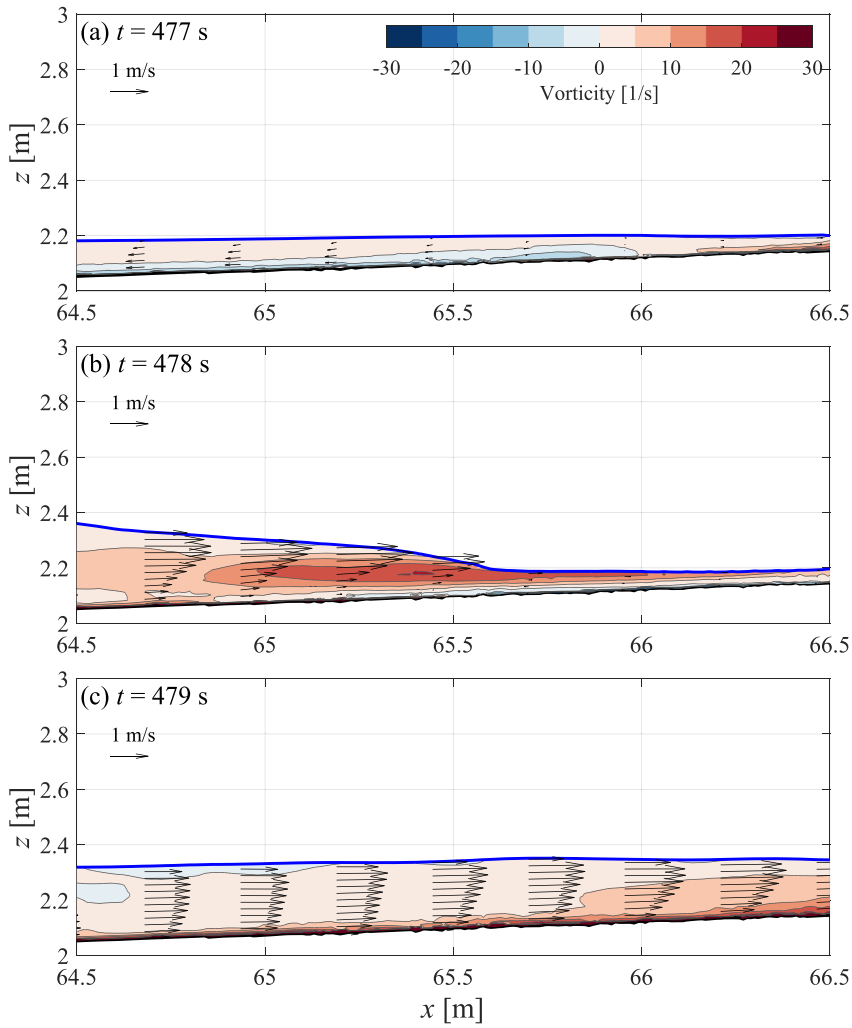

Figure 20. Spanwise averaged cross-shore velocity profiles for Case II at (a) t = 477.0 s, (b) t = 478.0 s, and (c) t = 479.0 s.

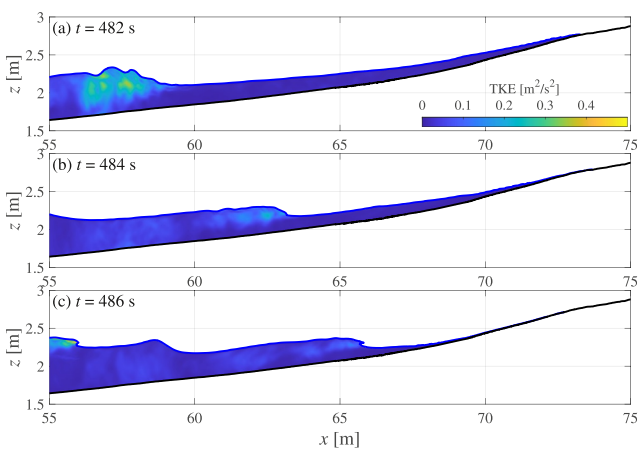

Figure 21. Turbulent kinetic energy in the swash zone for Case II at (a) t = 482.0 s, (b) t = 484.0 s, and (c) t = 486.0 s, respectively. The blue and black lines denote the free surface and bed profile correspondingly.

backwash boundary layer flow driving large offshore-directed bottom shear stress. The expected offshore transport is consistent with the continued expansion and offshore migration of the sandbar observed in the physical experiment (Figure 2a).

5. Discussion

A high value of the Shields parameter ($|\theta| > 1$) signifies the occurrence of sheet flow. The results demonstrate that large values of $|\theta|$ predominantly occur during the uprush and backwash phases. A comparative analysis between Cases I and II reveals that the maximum magnitudes of the time-averaged Shields parameter ($\overline{\theta}$) and the root-mean-square Shields parameter (θ_{rms}) in Case I slightly exceed those in Case II in their corresponding inner and swash zones, as shown in Figure 24b. Additionally, the calculated probability of sheet flow occurrence, $P(|\theta| > 1)$ — defined as the ratio of the number of instances where $|\theta| > 1$ to the total number of wave events — exhibits minimal differences between the two cases, with peak values around 55%, located slightly offshore from the mean water level line (Figure 24c).

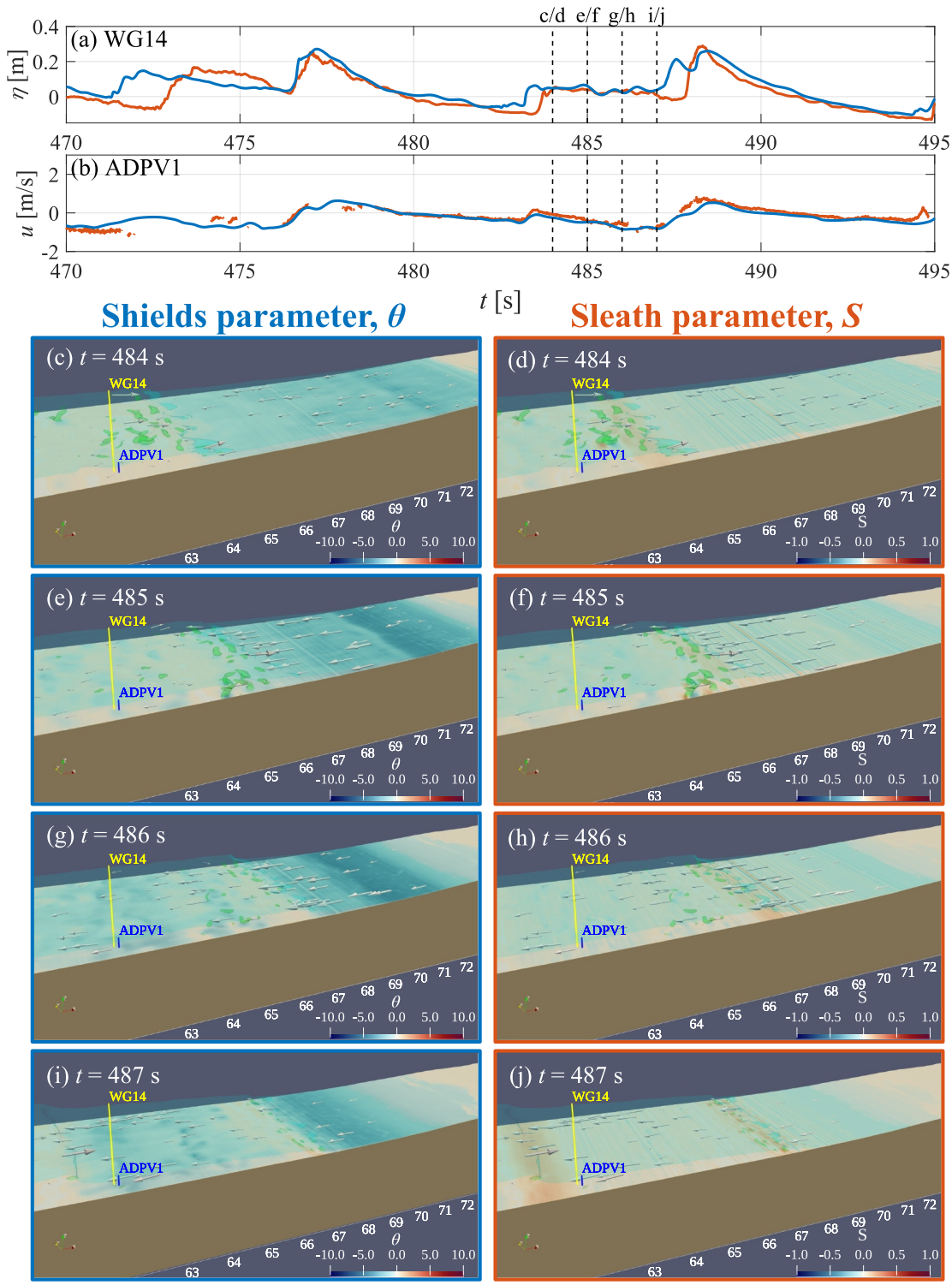

Figure 22. Time series of (a) free surface elevation and (b) streamwise flow velocity for a 30-s interval of Case II. The blue and orange lines denote numerical simulation and measured results, respectively. (c)–(j) Show the snapshots of the inner surf and swash zones at (c)–(d) $t = 484.0$ s, (e)–(f) $t = 485.0$ s, (g)–(h) $t = 486.0$ s, and (i)–(j) $t = 487.0$ s. The contour plot at the bed shows the Shields (c, e, g, i) and Sleath (d, f, h, j) parameters. The transparent cyan isosurface denotes free surface and the transparent green isosurface shows the turbulent coherent structures with a Q-criterion of 25.

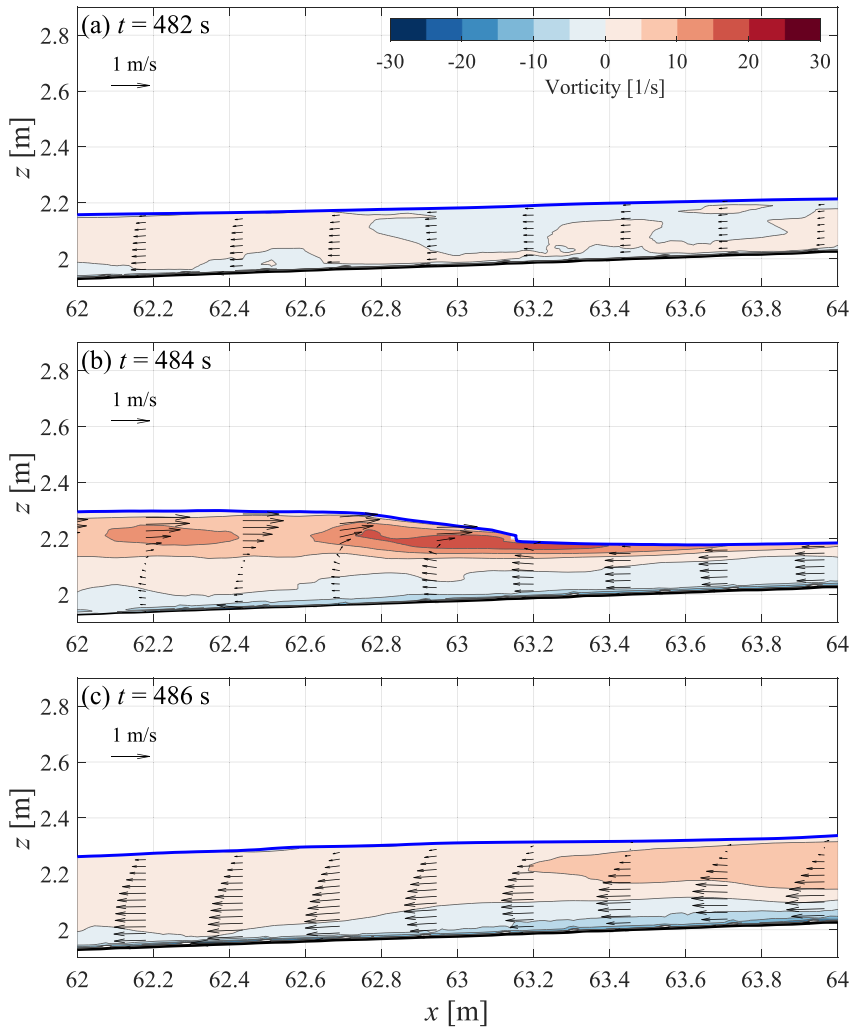

Figure 23. Spanwise averaged cross-shore velocity profiles for Case II at (a) t = 482.0 s, (b) t = 484.0 s, and (c) t = 486.0 s.

However, observations show that sheet flow dynamics contribute the largest portion of the total sediment transport load throughout the berm erosion (Pontiki et al., 2023). This implies some factors other than Shields parameter may play a role.

Applying analogous analytical methods to the Sleath parameter, using criteria of 0.1 and 0.29, yields notable contrasts. Specifically, $P(|S| > 0.1)$ in Case I ranges between 10% and 20% within the swash zone ($x \approx$ 64.3–65.8 m) and coincides with the berm front (Figure 24d). In contrast, Case II demonstrates nearly no occurrence of $|S| > 0.1$ in the swash zone ($x > 70$ m). Therefore, there is a 10%–20% likelihood of momentary bed failure at the berm front in Case I when applying a threshold of 0.1, as opposed to virtually no momentary bed failure in Case II. The frequency of strong wave-backwash interactions leading to momentary bed failure in Case I could potentially explain the observed berm erosion.

Additionally, the occurrence probabilities of $|S| > 0.29$ also vary between the cases, with Case I showing 1%–2% and Case II showing less than 0.5% (Figure 24e). Such interactions are predominantly attributed to direct collisions between the incoming waves and the backwash flow which is even more pronounced in the inner surf zone (see Section 4.1). In Case I, backwash flow separation occurs in the inner-surf zone due to wave-swash interaction (e.g., Figure 13b at $x \approx$ 58.4 m) and this is consistent with the results shown here that the occurrence probability of $|S| > 0.1$ is larger than 30% (or occurrence probability of $|S| > 0.29$ is 1%–2%) in the inner zone of $x \approx$ 57–62 m. In contrast, the occurrence probability of $|S| > 0.1$ is around 10% (or the occurrence probability of $|S| > 0.29$ is less than 0.5%) for Case II in the inner surf zone due to lack of wave-swash interaction. Despite the low percentage, the

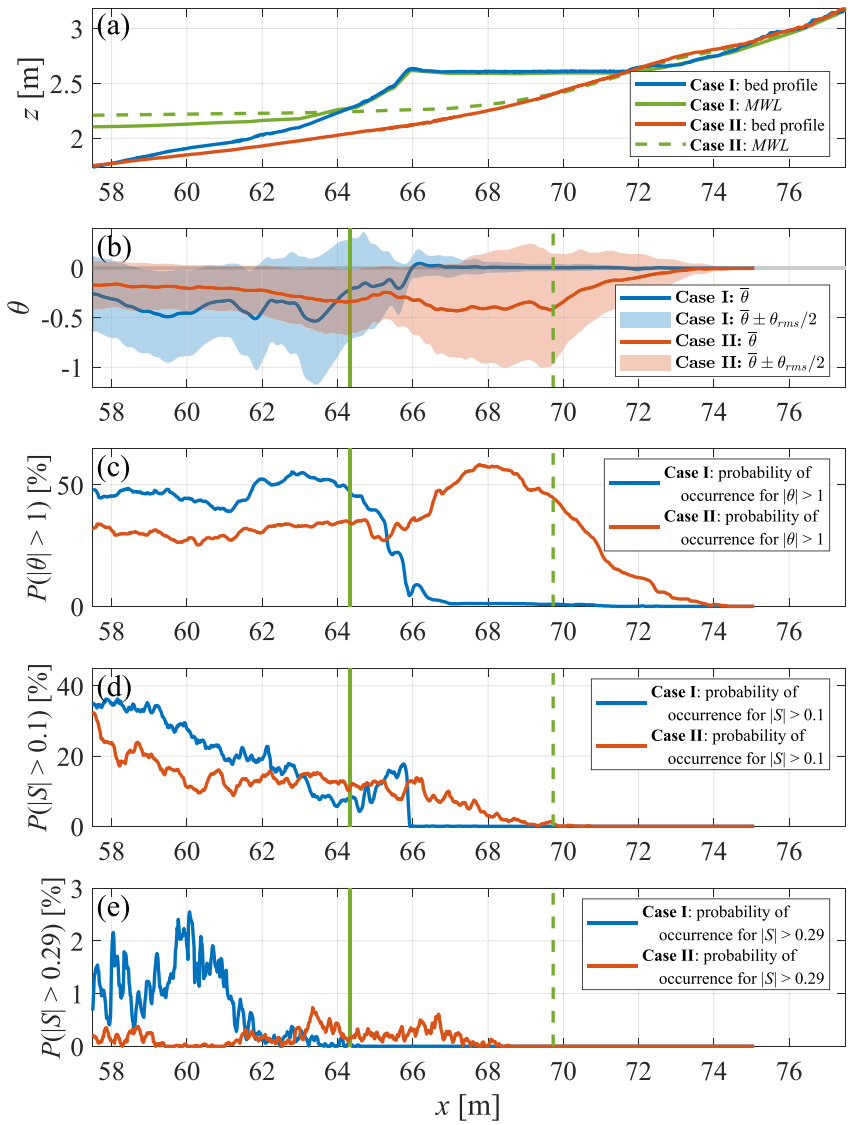

Figure 24. (a) Beach profiles and mean water levels in the swash zone. (b) Mean and root-mean-square Shields parameters. (c) Probability of occurrence of Shields parameter larger than 1. (d) Probability of occurrence of Sleath parameter larger than 0.1. (e) Probability of occurrence of Sleath parameter larger than 0.29. The green solid and dashed lines in panels (b), (c), (d), and (e) denote the shoreline position of the mean water level for Cases I and II, respectively.

impact of $|S| > 0.29$ on sediment transport in Case I is significant and should not be underestimated in terms of its contribution to net transport and beach morphodynamics.

Flow separation can suspend sediment from the bed and maintain them in the water column due to wave breaking/bore- and shear-layer-generated turbulence (Sou & Yeh, 2011). The occurrence of flow separation in Case I (Figures 13b and 17b) aligns with laboratory observations (Pujara et al., 2015; Sou & Yeh, 2011). In contrast, the absence of flow separation in Case II can be attributed to the lack of strong wave-backwash interactions.

In swash zones, direct turbulence-bed interactions become more pronounced compared to surf zones, where in the surf zone wave breaking-induced turbulence might not reach the bed due to greater water depths. The absence of a sandbar in Case I allows waves to break closer to the shoreline, enhancing wave-backwash interactions and resulting in higher levels of near-bed TKE in the swash zone, with peak values approximately 0.4–0.5 m^2/s^2 (Figure 14). Conversely, in Case II, wave breaking occurs offshore of the sandbar, resulting in lower near-bed TKE levels (approximately 0.05–0.15 m^2/s^2) located in the inner surf zone, rather than the swash zone

(Figure 21). These disparities in TKE and locations between the cases may be responsible for more pronounced erosion at the berm front in Case I compared to Case II.

Overall, Case I demonstrates a higher tendency for intense wave-backwash interactions compared to Case II, resulting in higher chance of momentary bed failure, near-bed TKE, and flow separation. These findings suggest that simulation and laboratory data collectively indicate a correlation between berm erosion (offshore sediment transport) and intense wave-backwash interactions.

6. Conclusions

A 3D LES coupled with a free surface tracking scheme was carried out to simulate cross-shore hydrodynamics, driven by random waves, in the inner surf and swash zone observed in a large wave flume experiment. The numerical model was validated with measured data with good agreements (overall Willmott's index of agreement greater than 0.8) for Cases I and II, which represented the hydrodynamics during berm erosion and subsequent sandbar formation, respectively.

In Case I, waves typically break closer to the shoreline, leading to a direct collision with the backwash flow. This proximity to the shoreline results in wave energy dissipation within a narrower surf zone, thereby increasing the likelihood of more energetic interactions. Conversely, in Case II, wave breaking predominantly occurs around the sandbar, leading to dissipation over a broader surf zone and consequently, a reduced probability of strong wave-backwash interaction events. Although the Shields parameter plays an important role in both Cases I and II, the intensity of the Sleath parameter is the key difference between these two cases. Higher probability of occurrence of large Sleath parameter ($P(|S| > 0.1)$) in Case I indicates the likely occurrence of momentary bed failure at the berm front, which may lead to berm erosion. In addition, flow separation also occurs during strong wave-backwash interaction that can enhance erosion and offshore sediment transport. Furthermore, the large TKE area in Case I located at the bore front, and has direct contact with the bed during uprush, may further contribute to sediment transport. Conversely, lower $P(|S| > 0.1)$ in Case II indicate that momentary bed failure is less likely to occur and sediment transport is mainly driven by bottom shear stress. The results also show no flow separation and relatively small near-bed TKE level in Case II.

These model simulations can help explain key mechanisms of steep berm erosion and offshore delivery of eroded sediment during the early stage of a storm when elevated water level (storm surge) causes waves to break closer to the berm and leads to more intense wave-backwash interactions. Thus, higher probability of occurrence of horizontal pressure gradient (Sleath parameter), flow separation, and stronger turbulence-berm interactions (high surface-generated TKE directly contacts the bed) appear which potentially cause berm erosion. Eroded sediment forms a sandbar that forces waves to break farther offshore leading to a energy dissipation over a broader surf zone. The subsequent bore entering the swash zone is much weaker and leads to less erosion of the beach face.

Data Availability Statement

Experimental data are available on the U.S. National Science Foundation Natural Hazards Engineering Research Infrastructure data depot, at https://doi.org/10.17603/ds2-csmw-8x65 (Pontiki & Puleo, 2023) and https://doi.org/10.17603/ds2-nf3k-fe18 (Bond & Wengrove, 2023).

Acknowledgments
This study was supported by the National Science Foundation under Grants 1519679, 1756714, 1756477, 1756449, and 2050854. The numerical simulations presented in this study were conducted on the Caviness and Darwin clusters at the University of Delaware and the Expanse cluster at the San Diego Supercomputer Center through ACCESS. We extend our gratitude to the developers of `OpenFOAM` and `waves2Foam` for their invaluable software. Special thanks are due to Daniel T. Cox and Rusty A. Feagin for their insightful contributions to this research. We also thank Johnathan L. Woodruff and Mark L. Buckley for the U.S. Geological Survey internal review of this manuscript, and the two anonymous reviewers whose feedback significantly enhanced this study. Lastly, any use of trade, firm, or product names is for descriptive purposes only and does not imply endorsement by the U.S. Government.

References

Alsina, J. M., Cáceres, I., Brocchini, M., & Baldock, T. E. (2012). An experimental study on sediment transport and bed evolution under different swash zone morphological conditions. *Coastal Engineering*, *68*, 31–43. https://doi.org/10.1016/j.coastaleng.2012.04.008

Altomare, C., Scandura, P., Cáceres, I., A, D. A. v. d., & Viccione, G. (2023). Large-scale wave breaking over a barred beach: SPH numerical simulation and comparison with experiments. *Coastal Engineering*, *185*, 104362. https://doi.org/10.1016/j.coastaleng.2023.104362

Battjes, J. A. (1974). Surf similarity. In *Proceedinds of the 14th International Conference on Coastal Engineering* (pp. 466–480). American Society of Civil Engineers. https://doi.org/10.1061/9780872621138.029

Berberović, E., van Hinsberg, N. P., Jakirlić, S., Roisman, I. V., & Tropea, C. (2009). Drop impact onto a liquid layer of finite thickness: Dynamics of the cavity evolution. *Physical Review E*, *79*(3), 036306. https://doi.org/10.1103/PhysRevE.79.036306

Bond, H., & Wengrove, M. (2023). Dune subsurface hydrodynamics during an extreme event. *Designsafe-CI*. https://doi.org/10.17603/DS2-NF3K-FE18

Bond, H., Wengrove, M., Puleo, J., Pontiki, M., Evans, T. M., & Feagin, R. A. (2023). Beach and dune subsurface hydrodynamics and their influence on the formation of dune scarps. *Journal of Geophysical Research: Earth Surface*, *128*(12), e2023JF007298. https://doi.org/10.1029/2023JF007298

Booij, N., Ris, R. C., & Holthuijsen, L. H. (1999). A third-generation wave model for coastal regions: 1. Model description and validation. *Journal of Geophysical Research*, *104*(C4), 7649–7666. https://doi.org/10.1029/98JC02622

Bouws, E., Günther, H., Rosenthal, W., & Vincent, C. L. (1985). Similarity of the wind wave spectrum in finite depth water: 1. Spectral form. *Journal of Geophysical Research*, *90*(C1), 975–986. https://doi.org/10.1029/JC090iC01p00975

Bradford, S. F. (2000). Numerical simulation of surf zone dynamics. *Journal of Waterway, Port, Coastal, and Ocean Engineering*, *126*(1), 1–13. https://doi.org/10.1061/(ASCE)0733-950X(2000)126:1(1)

Brown, S. A., Greaves, D. M., Magar, V., & Conley, D. C. (2016). Evaluation of turbulence closure models under spilling and plunging breakers in the surf zone. *Coastal Engineering*, *114*, 177–193. https://doi.org/10.1016/j.coastaleng.2016.04.002

Butt, T., Russell, P., Puleo, J., Miles, J., & Masselink, G. (2004). The influence of bore turbulence on sediment transport in the swash and inner surf zones. *Continental Shelf Research*, *24*(7), 757–771. https://doi.org/10.1016/j.csr.2004.02.002

Cáceres, I., & Alsina, J. M. (2012). A detailed, event-by-event analysis of suspended sediment concentration in the swash zone. *Continental Shelf Research*, *41*, 61–76. https://doi.org/10.1016/j.csr.2012.04.004

Cebeci, T., & Bradshaw, P. (1977). *Momentum transfer in boundary layers* (1st ed.). Hemisphere Publishing Corporation.

Christensen, E. D. (2006). Large eddy simulation of spilling and plunging breakers. *Coastal Engineering*, *53*(5), 463–485. https://doi.org/10.1016/j.coastaleng.2005.11.001

Christensen, E. D., & Deigaard, R. (2001). Large eddy simulation of breaking waves. *Coastal Engineering*, *42*(1), 53–86. https://doi.org/10.1016/S0378-3839(00)00049-1

Derakhti, M., & Kirby, J. T. (2014). Bubble entrainment and Liquid–Bubble interaction under unsteady breaking waves. *Journal of Fluid Mechanics*, *761*, 464–506. https://doi.org/10.1017/jfm.2014.637

Derakhti, M., Kirby, J. T., Shi, F., & Ma, G. (2016). Wave breaking in the surf zone and deep-water in a non-hydrostatic rans model. Part 2: Turbulence and mean circulation. *Ocean Modelling*, *107*, 139–150. https://doi.org/10.1016/j.ocemod.2016.09.011

Elgar, S., & Guza, R. T. (1985). Observations of bispectra of shoaling surface gravity waves. *Journal of Fluid Mechanics*, *161*(-1), 425–448. https://doi.org/10.1017/S0022112085003007

Feagin, R. A., Innocenti, R. A., Bond, H., Wengrove, M., Huff, T. P., Lomonaco, P., et al. (2023). Does vegetation accelerate coastal dune erosion during extreme events? *Science Advances*, *9*(24), eadg7135. https://doi.org/10.1126/sciadv.adg7135

Florence, M., Stark, N., Raubenheimer, B., & Elgar, S. (2022). Nearshore vertical pore pressure gradients and onshore sediment transport under tropical storm forcing. *Journal of Waterway, Port, Coastal, and Ocean Engineering*, *148*(6), 04022023. https://doi.org/10.1061/(ASCE)WW.1943-5460.0000723

Foster, D. L., Bowen, A. J., Holman, R. A., & Natoo, P. (2006). Field evidence of pressure gradient induced incipient motion. *Journal of Geophysical Research*, *111*(C5). https://doi.org/10.1029/2004JC002863

Fuhrman, D. R., & Li, Y. (2020). Instability of the realizable k-ε turbulence model beneath surface waves. *Physics of Fluids*, *32*(11), 115108. https://doi.org/10.1063/5.0029206

Higuera, P., Lara, J. L., & Losada, I. J. (2013). Simulating coastal engineering processes with OpenFOAM®. *Coastal Engineering*, *71*, 119–134. https://doi.org/10.1016/j.coastaleng.2012.06.002

Hirt, C. W., & Nichols, B. D. (1981). Volume of fluid (VOF) method for the dynamics of free boundaries. *Journal of Computational Physics*, *39*(1), 201–225. https://doi.org/10.1016/0021-9991(81)90145-5

Hughes, M. G., & Moseley, A. S. (2007). Hydrokinematic regions within the swash zone. *Continental Shelf Research*, *27*(15), 2000–2013. https://doi.org/10.1016/j.csr.2007.04.005

Hunt, J. C. R., Wray, A. A., & Moin, P. (1988). Eddies, streams, and convergence zones in turbulent flows. In studying turbulence using numerical simulation databases, 2. In *Proceedings of the 1988 summer program* (pp. 193–208). Center for Turbulence Research. Retrieved from https://ntrs.nasa.gov/citations/19890015184

Innocenti, R. A., Feagin, R. A., Charbonneau, B. R., Figlus, J., Lomonaco, P., Wengrove, M., et al. (2021). The effects of plant structure and flow properties on the physical response of coastal dune plants to wind and wave run-up. Estuarine. *Coastal and Shelf Science*, *261*, 107556. https://doi.org/10.1016/j.ecss.2021.107556

Jacobsen, N. G., Fuhrman, D. R., & Fredsøe, J. (2012). A wave generation toolbox for the open-source CFD library: OpenFOAM®. *International Journal for Numerical Methods in Fluids*, *70*(9), 1073–1088. https://doi.org/10.1002/fld.2726

Kim, Y., Zhou, Z., Hsu, T.-J., & Puleo, J. A. (2017). Large eddy simulation of dam-break-driven swash on a rough-planar beach. *Journal of Geophysical Research: Oceans*, *122*(2), 1274–1296. https://doi.org/10.1002/2016JC012366

Lakehal, D., & Liovic, P. (2011). Turbulence structure and interaction with steep breaking waves. *Journal of Fluid Mechanics*, *674*, 522–577. https://doi.org/10.1017/jfm.2011.3

Larsen, B. E., & Fuhrman, D. R. (2018). On the over-production of turbulence beneath surface waves in Reynolds-averaged Navier–Stokes models. *Journal of Fluid Mechanics*, *853*, 419–460. https://doi.org/10.1017/jfm.2018.577

Larsen, B. E., van der A, D. A., van der Zanden, J., Ruessink, G., & Fuhrman, D. R. (2020). Stabilized rans simulation of surf zone kinematics and boundary layer processes beneath large-scale plunging waves over a breaker bar. *Ocean Modelling*, *155*, 101705. https://doi.org/10.1016/j.ocemod.2020.101705

Li, Y., Larsen, B. E., & Fuhrman, D. R. (2022). Reynolds stress turbulence modelling of surf zone breaking waves. *Journal of Fluid Mechanics*, *937*, A7. https://doi.org/10.1017/jfm.2022.92

Lin, P., & Liu, P. L.-F. (1998). A numerical study of breaking waves in the surf zone. *Journal of Fluid Mechanics*, *359*, 239–264. https://doi.org/10.1017/S002211209700846X

Liu, P. L.-F., & Losada, I. J. (2002). Wave propagation modeling in coastal engineering. *Journal of Hydraulic Research*, *40*(3), 229–240. https://doi.org/10.1080/00221680209499939

Lowe, R. J., Buckley, M. L., Altomare, C., Rijnsdorp, D. P., Yao, Y., Suzuki, T., & Bricker, J. D. (2019). Numerical simulations of surf zone wave dynamics using smoothed particle hydrodynamics. *Ocean Modelling*, *144*, 101481. https://doi.org/10.1016/j.ocemod.2019.101481

Lubin, P., Vincent, S., Abadie, S., & Caltagirone, J.-P. (2006). Three-dimensional large eddy simulation of air entrainment under plunging breaking waves. *Coastal Engineering*, *53*(8), 631–655. https://doi.org/10.1016/j.coastaleng.2006.01.001

Ma, G., Shi, F., & Kirby, J. T. (2012). Shock-capturing non-hydrostatic model for fully dispersive surface wave processes. *Ocean Modelling*, *43–44*, 22–35. https://doi.org/10.1016/j.ocemod.2011.12.002

Madsen, P. A., & Sørensen, O. R. (1992). A New form of the Boussinesq equations with improved linear dispersion characteristics. Part 2. A slowly-varying bathymetry. *Coastal Engineering*, *18*(3), 183–204. https://doi.org/10.1016/0378-3839(92)90019-Q

Mayer, S., & Madsen, P. A. (2000). Simulation of breaking waves in the surf zone using a Navier-Stokes solver. In *Proc., 27th international conference on coastal engineering* (pp. 928–941). American Society of Civil Engineers. https://doi.org/10.1061/40549(276)72

O'Donoghue, T., Pokrajac, D., & Hondebrink, L. J. (2010). Laboratory and numerical study of dambreak-generated swash on impermeable slopes. *Coastal Engineering*, *57*(5), 513–530. https://doi.org/10.1016/j.coastaleng.2009.12.007

Olabarrieta, M., Warner, J. C., & Hegermiller, C. A. (2023). Development and application of an Infragravity Wave (InWave) driver to simulate nearshore processes. *Journal of Advances in Modeling Earth Systems*, *15*(6), e2022MS003205. https://doi.org/10.1029/2022MS003205

Pontiki, M., & Puleo, J. (2023). Sediment transport processes across a rapidly eroding bare dune. *Designsafe-CI*. https://doi.org/10.17603/DS2-CSMW-8X65

Pontiki, M., Puleo, J. A., Bond, H., Wengrove, M., Feagin, R. A., Hsu, T.-J., & Huff, T. P. (2023). Geomorphic response of a coastal berm to storm surge and the importance of sheet flow dynamics. *Journal of Geophysical Research: Earth Surface*, *128*(10), e2022JF006948. https://doi.org/10.1029/2022JF006948

Pujara, N., Liu, P. L.-F., & Yeh, H. H. (2015). An experimental study of the interaction of two successive solitary waves in the swash: A strongly interacting case and a weakly interacting case. *Coastal Engineering*, *105*, 66–74. https://doi.org/10.1016/j.coastaleng.2015.07.011

Puleo, J. A., Beach, R. A., Holman, R. A., & Allen, J. S. (2000). Swash zone sediment suspension and transport and the importance of bore-generated turbulence. *Journal of Geophysical Research*, *105*(C7), 17021–17044. https://doi.org/10.1029/2000JC900024

Rafati, Y., Hsu, T.-J., Elgar, S., Raubenheimer, B., Quataert, E., & van Dongeren, A. (2021). Modeling the hydrodynamics and morphodynamics of sandbar migration events. *Coastal Engineering*, *166*, 103885. https://doi.org/10.1016/j.coastaleng.2021.103885

Roelvink, D., Reniers, A., van Dongeren, A., de Vries, J. V. T., McCall, R., & Lescinski, J. (2009). Modelling storm impacts on beaches, dunes and barrier Islands. *Coastal Engineering*, *56*(11), 1133–1152. https://doi.org/10.1016/j.coastaleng.2009.08.006

Rusche, H. (2002). *Computational fluid dynamics of dispersed two-phase flows at high phase fractions* (Ph.D. Thesis). Imperial College London. Retrieved from http://hdl.handle.net/10044/1/8110

Sallenger, A. H. (2000). Storm impact scale for barrier islands. *Journal of Coastal Research*, *16*(3), 890–895. Retrieved from https://www.jstor.org/stable/4300099

Shih, T.-H., Liou, W. W., Shabbir, A., Yang, Z., & Zhu, J. (1995). A New k-ε eddy viscosity model for high Reynolds number turbulent flows. *Computers & Fluids*, *24*(3), 227–238. https://doi.org/10.1016/0045-7930(94)00032-T

Sleath, J. F. A. (1999). Conditions for plug formation in oscillatory flow. *Continental Shelf Research*, *19*(13), 1643–1664. https://doi.org/10.1016/S0278-4343(98)00096-X

Smagorinsky, J. (1963). General circulation experiments with the primitive equations: I. The basic experiment. *Monthly Weather Review*, *91*(3), 99–164. https://doi.org/10.1175/1520-0493(1963)091⟨0099:GCEWTP⟩2.3.CO;2

Sou, I. M., Cowen, E. A., & Liu, P. L.-F. (2010). Evolution of the turbulence structure in the surf and swash zones. *Journal of Fluid Mechanics*, *644*, 193–216. https://doi.org/10.1017/S0022112009992321

Sou, I. M., & Yeh, H. (2011). Laboratory study of the cross-shore flow structure in the surf and swash zones. *Journal of Geophysical Research*, *116*(C3), C03002. https://doi.org/10.1029/2010JC006700

Sumer, B. M., Guner, H. A. A., Hansen, N. M., Fuhrman, D. R., & Fredsøe, J. (2013). Laboratory observations of flow and sediment transport induced by plunging regular waves. *Journal of Geophysical Research: Oceans*, *118*(11), 6161–6182. https://doi.org/10.1002/2013JC009324

Sussman, M., Smereka, P., & Osher, S. (1994). A level set approach for computing solutions to incompressible two-phase flow. *Journal of Computational Physics*, *114*(1), 146–159. https://doi.org/10.1006/jcph.1994.1155

Symonds, G., Huntley, D. A., & Bowen, A. J. (1982). Two-dimensional surf beat: Long wave generation by a time-varying breakpoint. *Journal of Geophysical Research*, *87*(C1), 492–498. https://doi.org/10.1029/JC087iC01p00492

Tolman, H. L. (1991). A third-generation model for wind waves on slowly varying, unsteady, and inhomogeneous depths and currents. *Journal of Physical Oceanography*, *21*(6), 782–797. https://doi.org/10.1175/1520-0485(1991)021⟨0782:ATGMFW⟩2.0.CO;2

Tsai, B. (2023). *Coastal hydrodynamics and its interaction with structure and sediment* (Ph.D. Dissertation). University of Delaware. https://doi.org/10.58088/evz4-5f03

van Rijn, L. C., Tonnon, P. K., Sánchez-Arcilla, A., Cáceres, I., & Grüne, J. (2011). Scaling laws for beach and dune erosion processes. *Coastal Engineering*, *58*(7), 623–636. https://doi.org/10.1016/j.coastaleng.2011.01.008

Watanabe, Y., Saeki, H., & Hosking, R. J. (2005). Three-dimensional vortex structures under breaking waves. *Journal of Fluid Mechanics*, *545*, 291–328. https://doi.org/10.1017/S0022112005006774

Wei, G., Kirby, J. T., Grilli, S. T., & Subramanya, R. (1995). A fully nonlinear Boussinesq model for surface waves. Part 1. Highly nonlinear unsteady waves. *Journal of Fluid Mechanics*, *294*, 71–92. https://doi.org/10.1017/S0022112095002813

Wei, Z., Dalrymple, R. A., Xu, M., Garnier, R., & Derakhti, M. (2017). Short-crested waves in the surf zone. *Journal of Geophysical Research: Oceans*, *122*(5), 4143–4162. https://doi.org/10.1002/2016JC012485

Willmott, C. J. (1981). On the validation of models. *Physical Geography*, *2*(2), 184–194. https://doi.org/10.1080/02723646.1981.10642213

Xie, Z. (2013). Two-phase flow modelling of spilling and plunging breaking waves. *Applied Mathematical Modelling*, *37*(6), 3698–3713. https://doi.org/10.1016/j.apm.2012.07.057

Zelt, J. A., & Skjelbreia, J. E. (1992). Estimating incident and reflected wave fields using an arbitrary number of wave gauges. In *Proceedings of the 23th international conference on coastal engineering* (pp. 777–789). American Society of Civil Engineers. https://doi.org/10.1061/9780872629332.058

Zhou, Z., Hsu, T.-J., Cox, D., & Liu, X. (2017). Large-eddy simulation of wave-breaking induced turbulent coherent structures and suspended sediment transport on a barred beach. *Journal of Geophysical Research: Oceans*, *122*(1), 207–235. https://doi.org/10.1002/2016JC011884

Zhou, Z., Sangermano, J., Hsu, T.-J., & Ting, F. C. K. (2014). A numerical investigation of wave-breaking-induced turbulent coherent structure under a solitary wave. *Journal of Geophysical Research: Oceans*, *119*(10), 6952–6973. https://doi.org/10.1002/2014JC009854

Zijlema, M., Stelling, G., & Smit, P. (2011). SWASH: An operational public domain code for simulating wave fields and rapidly varied flows in coastal waters. *Coastal Engineering*, *58*(10), 992–1012. https://doi.org/10.1016/j.coastaleng.2011.05.015